RSC Advances

PAPER

View Article Online
View Journal | View Issue

Cite this: *RSC Adv.*, 2026, **16**, 24964

Integrated structural, vibrational, thermal, and optical characterization of a zinc-based organic–inorganic hybrid with DFT and molecular docking insights into its biological properties

Houyem Khlifi,[a] Mashael A. Alghamdi,[b] Intissar Tababi,[a] Hayet Edziri,[c] Marwa Melliti,[c] Ahlem Guesmi,[b] Hossam H. Nasrallah,[d] Noureddine Mhadhbi,[ae] Naoufel Ben Hamadi[b] and Houcine Naïli*[a]

Received 13th April 2026
Accepted 27th April 2026

DOI: 10.1039/d6ra03131e

rsc.li/rsc-advances

A novel zero-dimensional organic–inorganic hybrid material, $(C_9H_8N)_2[ZnCl_4]\cdot 2H_2O$, was synthesized and investigated using structural, spectroscopic, thermal, optical, and biological approaches. Single-crystal X-ray diffraction reveals a monoclinic structure ($C2/c$) composed of isolated $[ZnCl_4]^{2-}$ tetrahedra stabilized by quinolinium cations and lattice water molecules through hydrogen bonding and π–π interactions. Vibrational analyses (FTIR and Raman) confirm the structural features and indicate slight distortions of the $ZnCl_4^{2-}$ units. Thermal studies show a multistep decomposition involving dehydration followed by organic framework degradation. Optical investigations based on diffuse reflectance spectroscopy reveal an indirect band gap ($E_g \approx 3.02$ eV), with electronic transitions dominated by $\pi \rightarrow \pi^*$ and ligand-to-metal charge transfer processes. Density Functional Theory (DFT) calculations at the B3LYP/6-31G(d) level confirm the electronic stability of the complex, exhibiting a moderate energy gap consistent with its semiconducting behavior. *In silico* ADME analysis suggests acceptable drug-likeness, high gastrointestinal absorption, and favorable pharmacokinetic characteristics. Molecular docking studies toward DNA gyrase and LasR proteins reveal moderate binding affinities relative to Ciprofloxacin, supporting the experimentally observed antibacterial activity. Furthermore, the compound exhibits significant antibacterial and antibiofilm activities against both Gram-positive and Gram-negative bacteria. These findings highlight the multifunctional character of this zinc-based hybrid material, combining structural stability, semiconducting behavior, and promising biological activity.

1 Introduction

Organic–inorganic hybrid materials have attracted considerable attention due to their structural diversity and the possibility of tailoring their physicochemical properties through the combination of inorganic frameworks and functional organic cations. Early studies in this field focused on inorganic semiconductors such as TiO_2 and ZnO, widely investigated for their photocatalytic activity and stability.[1] However, these systems are often limited by wide band gaps and rapid charge recombination,[2,3] motivating the development of alternative materials with improved optical and electronic properties.

In this context, organic–inorganic halometallates have emerged as a versatile class of hybrid materials.[4–9] These compounds, typically composed of discrete inorganic units such as $[MX_4]^{2-}$ or $[MX_6]^{2-}$ combined with organic cations, exhibit tunable structures and interesting optical behavior.[10] In particular, zero-dimensional tetrahalometallates have gained attention due to their localized electronic states and potential applications in optoelectronics and photonic materials.[11,12] Recent studies have highlighted their relevance for energy-related applications,[13–15] although their functional properties remain less explored compared to conventional systems.

Zinc-based halometallates represent an important subclass within this family. The Zn^{2+} ion, with its d^{10} electronic configuration and low toxicity, readily forms stable tetrahedral $[ZnCl_4]^{2-}$ units that can be incorporated into hybrid structures with various organic cations. Several compounds based on $[ZnCl_4]^{2-}$ anions have been reported, particularly with nitrogen-

---

[a] Laboratory Physical-Chemistry of the Solid State, Department of Chemistry, Faculty of Sciences of Sfax, B.P. 1171, Sfax 3000, University of Sfax, Tunisia. E-mail: houcine_naili@yahoo.com

[b] Chemistry Department, College of Science, Imam Mohammad Ibn Saud Islamic University (IMSIU), Riyadh 11623, Saudi Arabia

[c] Laboratory of Transmissible Diseases and Biologically Active Substances (LR99ES27), Faculty of Pharmacy, University of Monastir, Monastir, Tunisia

[d] Chemistry Department, Faculty of Biotechnology, Sinai University, Kantara 41632, Egypt

[e] University of Monastir, Preparatory Institute for Engineering Studies of Monastir, Monastir 5019, Tunisia

containing heterocycles such as benzimidazolium and pyridinium derivatives, leading to diverse structural architectures and physicochemical properties.[16,17] Nevertheless, systematic investigations correlating their structure with functional properties remain limited.[18–24]

Among potential organic cations, quinoline derivatives are particularly attractive due to their extended π-conjugated systems and their ability to engage in hydrogen bonding and π–π stacking interactions. In addition to their structural role, quinolinium-based systems have demonstrated notable photophysical and catalytic properties, including applications in photocatalytic transformations and oxidation reactions.[25–28] These features make them promising candidates for the design of multifunctional hybrid materials.

Despite these advantages, the integration of quinolinium cations with tetrahalozincate anions remains insufficiently explored. In particular, structurally characterized hybrids combining quinolinium and $[ZnCl_4]^{2-}$ units are rare, and studies linking their structural organization to optical and biological properties are still lacking. This gap highlights the need for further investigation of such systems.

In this work, we report the synthesis and comprehensive characterization of a new organic–inorganic hybrid compound, $(C_9H_8N)_2[ZnCl_4]\cdot 2H_2O$. The structure consists of isolated $[ZnCl_4]^{2-}$ tetrahedra stabilized by protonated quinolinium cations and lattice water molecules through hydrogen bonding and π–π interactions. A combination of single-crystal X-ray diffraction, vibrational spectroscopy, thermal analysis, and diffuse reflectance spectroscopy was used to investigate its structural and optical properties. In addition, density functional theory (DFT) calculations and molecular docking studies were performed to explore its electronic structure and potential biological activity.

2 Experimental section

2.1 Chemical materials

For the present experiment, reagents of analytical grade were employed as supplied by Sigma-Aldrich: zinc chloride ($ZnCl_2$, 99% purity), quinoline (C_9H_7N, 98% purity), and hydrochloric acid (HCl, 37%).

2.2 Synthesis of $(C_9H_8N)_2[ZnCl_4]\cdot 2H_2O$

Quinoline and ethanol were utilized as received from commercial suppliers without further purification. The reaction was conducted under an inert atmosphere of high-purity nitrogen employing standard Schlenk techniques. A solution of quinoline (0.258 g, 2 mmol) in 10 mL of absolute ethanol was prepared and subsequently combined with zinc chloride ($ZnCl_2$, 0.136 g, 1 mmol) and 1 mL of 37% aqueous hydrochloric acid in a glass vessel maintained at 60 °C in an oil bath. Complete dissolution of the reactants was achieved after more than 2 h. The mixture was filtered and gradually cooled in the oil bath, after which it was left to stand at ambient temperature until most of the solvent had evaporated. The resulting colorless, plate-shaped crystals were isolated and dried in a desiccator. Elem. Microanal. Obsd for $(C_9H_8N)_2[ZnCl_4]\cdot 2H_2O$ (calcd): C, 11.55 (11.48); H, 2.42 (2.37); N, 8.21 (8.10). (IR, KBr, cm^{-1}): ν(N–H$^+$), 1529; ν(C–N), 1643. The yield of the reaction was 0.488 g (97%). ESI MASS m/z [M − H]-calcd 503.22, found 503.53.

2.3 Single-crystal X-ray data collection and structure determination

A single crystal, approximately 0.39 × 0.27 × 0.06 mm^3, was used to collect diffraction data at 150 K with an Xcalibur Atlas Gemini Ultra diffractometer utilizing Mo-Kα radiation (λ = 0.71073 Å) and processed through the SCALE3 ABSPACK[29] program. Data collection, reduction, and analysis were conducted using SAINT,[30] with semi-empirical multi-scan absorption corrections applied *via* the SADABS[31] program. The crystal structure was determined in the monoclinic space group $C2/c$ using auto-methods available in WINGX.[32] The structure of $(C_9H_8N)_2[ZnCl_4]\cdot 2H_2O$ was solved by the dual-space algorithm using SHELXT-2015 (ref. 33) and refined by full-matrix least-squares techniques using SHELXL[33] with anisotropic thermal parameters for all non-hydrogen atoms. All figures were prepared using DIAMOND.[34] The refinement conditions and structural resolution of the compound are outlined in Table S1.

2.4 Thermal analysis

The thermal decomposition behavior of the $(C_9H_8N)_2[ZnCl_4]\cdot 2H_2O$ complex was examined through simultaneous thermogravimetric analysis (TGA) and differential thermal analysis (DTA) under oxygen atmosphere (flow rate: 100 mL min^{-1}) using a SETARAM TG–DSC 92 instrument. The analysis was performed on a 2.687 mg sample, with thermograms recorded over a temperature range of 25–400 °C for DSC and 25–650 °C for TGA, applying a constant heating rate of 10 °C min^{-1}.

2.5 Spectroscopic measurement

Infrared (IR) measurements were performed over the 400–4000 cm^{-1} range using a PerkinElmer Spectrum 400 FTIR spectrometer operating in UATR (Universal Attenuated Total Reflectance) mode. Raman spectra were acquired independently in the 0–3500 cm^{-1} region using a Horiba LabRAM HR Evolution system with a 532 nm laser as the excitation source.

2.6 UV-vis-NIR diffuse reflectance spectroscopy

The UV-vis diffuse reflectance spectrum of the $(C_9H_8N)_2[ZnCl_4]\cdot 2H_2O$ compound was performed at room temperature using a Varian Cary 5000 UV-vis-NIR spectrophotometer in the wavelength range between 200 and 800 nm.

2.7 *In Silico* studies

Density Functional Theory (DFT) calculations were performed at the B3LYP/6-31G(d) level of theory to optimize the molecular geometry of the investigated complex. The optimized structure was subsequently used to analyze frontier molecular orbitals (HOMO and LUMO), the energy gap (ΔE), and molecular electrostatic potential (MEP) maps, providing insight into the electronic structure and potential reactive sites.[35–37]

Drug-likeness, physicochemical properties, and pharmacokinetic parameters were predicted using the SwissADME platform.[38] Canonical SMILES representations were used to calculate molecular weight, lipophilicity (Log P), hydrogen bond donors and acceptors, and topological polar surface area (TPSA). Drug-likeness was evaluated based on Lipinski's rule of five, as well as Veber and Ghose criteria.

Pharmacokinetic properties were further evaluated using the pkCSM web server. The predicted parameters included water solubility (log mol L^{-1}), Caco-2 permeability (log P_{app} in 10^{-6} cm s^{-1}), intestinal absorption (%), skin permeability (log K_p), and P-glycoprotein (P-gp) interactions, including substrate behavior and inhibitory effects on P-gp I and P-gp II.

Molecular docking was performed to evaluate the interaction of the $(C_9H_8N)_2[ZnCl_4]\cdot 2H_2O$ complex with key bacterial targets, namely DNA Gyrase and LasR. The crystal structures were obtained from the Protein Data Bank (PDB IDs: 1AB4 and 3IX3, respectively).[39,40]

Protein structures were prepared by removing crystallographic water molecules, adding hydrogen atoms, and performing energy minimization.[41] The ligand structure was geometry-optimized prior to docking. Docking simulations were carried out using AutoDock Vina 1.1.2.[42] The binding site was defined based on the position of the co-crystallized ligand, and the best binding poses were selected according to the lowest binding energy.[40,43,44] For validation purposes, Ciprofloxacin was used as a reference (control) ligand for DNA gyrase. Protein–ligand interactions, including hydrogen bonding and hydrophobic contacts, were analyzed and visualized using PyMOL Molecular Graphics System (Version 2.5).[45]

2.8 Evaluation of the antibacterial activity

The antibacterial aspects of several common microbes have been assessed, including *Pseudomonas aeruginosa*, *Escherichia coli*, *Staphylococcus aureus*, and *Enterococcus faecalis*. These pathogens were supplied by the microbiology lab at Fattouma Bourguiba Hospital. Using the microdilution method, the sample's minimum inhibitory concentration (MIC) was determined. All of the produced samples were diluted in 10% DMSO. The 96-well plates were then subjected to cascade dilutions using DMSO (10%). Then, 100 µL of brain-heart broth and 20 µL of overnight culture (adjusted to McFarland turbidity of 0.5) were added. The plates were incubated at 37 °C for 24 hours. The MIC was the lower concentration of the sample that stopped all observable growth. 5 µL was reinoculated in Brain Heart Agar plates for 24 hours from each well that did not show any growth in order to determine the minimum bactericidal concentration (MBC). Ciprofloxacin was used as the positive control for the antibacterial activity.[46]

2.9 Antibiofilm test

This experiment was established against the bacteria *Staphylococcus aureus* (*S. aureus*), *Enterococcus faecalis* (*E. faecalis*), *Escherichia coli* (*E. coli*), and *Pseudomonas aeruginosa* (*P. aeruginosa*) .The modified micro dilution method was utilized. Overnight-grown cultures in Brain Heart Infusion (BHI) were diluted to 10^6 CFU mL^{-1} in BHI and 2% (w/v) glucose. An aliquot (200 µL) was transferred to a 96-well microtiter plate, and 100 µL of samples with final concentrations corresponding to MIC, 2× MIC, and 4× MIC were added.[47] The sample-free media was used as a control. Every experiment was conducted in triplicate. The culture supernatant was discarded after a 24 hours incubation period at 37 °C, and non-adherent cells were removed from the wells by washing them with phosphate-buffered saline. The surface-attached cells were stained for 15 minutes using 200 µL of 0.1% crystal violet, followed by rinsing with water to remove excess stain. A Multiskan reader (BioRad, Tokyo, Japan) was used to assess biofilm cells colored with crystal violet at 570 nm.[47] The biofilm inhibition percentage was determined using the equation below:

Table 1 Normalized EE (λ) × I(λ) values used in SPF calculation

λ (nm)	EE(λ) × I(λ) (normalised)
290	0.015
295	0.0817
300	0.2874
305	0.3278
310	0.1864
315	0.0837
320	0.018
Total	1

Table 2 SPF values and corresponding percent UV blocking

SPF value	% of UV blocking
2	50
4	75
5	80
10	90
15	93
25	96

$$\text{Biofilm inhibition } (\%) = \frac{OD_{gc} - OD_s}{OD_{gc}} \text{ x } 100$$

where OD_s (sample) represents the absorbance of the compound with bacteria and OD_{gc} (growth control) is the absorbance of the bacteria's growth without the sample.

2.10 Evaluation of the photoprotective activity

The extract was used to determine the SPF value. The spectrophotometric absorbance of the extracts was really measured in the UV-B wavelength region (290–320 nm) at dosages of 0.2 and 1 mg mL^{-1}.[48] The *in vitro* SPF values were calculated using the Mansur *et al.* equation.[49] The findings were displayed using the mean ± standard deviation of three repeats ($n = 3$).

$SPF = I(\lambda)$, $Abs(\lambda)$, $CF \times \sum 320\ 290\ EE(\lambda)$ (Table 1). The table displays the $EE(\lambda) \times I(\lambda)$ values, where $EE(\lambda)$ represents the erythemogenic effect of radiation at λ, $I(\lambda)$ represents the intensity of solar light at λ, $Abs(\lambda)$ represents the absorbance of the preparation at λ, and CF is the correction factor that was found to provide an SPF value of 4 for the reference formulation containing 2.7% octyl methoxycinnamate(Table 2).

3 Results and discussion

3.1 Structural study

Fig. 1 presents the structural formulation and asymmetric unit of the newly synthesized zero-dimensional hybrid material $(C_9H_8N)_2[ZnCl_4]\cdot 2H_2O$, as generated by Diamond 3. The asymmetric unit, shown in full opacity, corresponds to one half of the crystallographically independent content, while the complete formula unit, displayed with partial transparency, arises from the application of the crystallographic symmetry operations of the monoclinic *C*2/*c* space group. At the core of the structure, the Zn^{2+} center is tetrahedrally coordinated by four chloride ligands, forming the discrete $[ZnCl_4]^{2-}$ anion, a strictly zero-dimensional inorganic entity with no extended connectivity beyond its coordination sphere. This anion is electrostatically balanced by two quinolinium cations, whose protonated nitrogen atoms facilitate strong hydrogen-bonding and electrostatic interactions with both the inorganic fragment and the solvation water molecules. The latter, present as two discrete H_2O units per formula, play a stabilizing role by extending the hydrogen-bond network, thus reinforcing the cohesion of the crystal packing. A noteworthy crystallographic feature is the presence of a twofold rotation axis passing through the Zn atom, highlighted in the figure by a line intersecting the tetrahedral center, which reflects the symmetry operations inherent to the *C*2/*c* space group. This combined representation of asymmetric and formula units emphasizes the dual organic–inorganic nature of the compound and the structural compactness imposed by both electrostatic and hydrogen-bonding interactions. The clear definition of the asymmetric unit and its symmetry-related counterparts establishes the foundation for subsequent discussion of the packing arrangements, coordination geometry distortions, and supramolecular interactions that will be explored in Fig. 2 through 6.

Fig. 2 presents the crystal packing of $(C_9H_8N)_2[ZnCl_4]\cdot 2H_2O$ projected along the *a*, *b*, and *c* axes, highlighting how the discrete components organize within the monoclinic lattice. The projections confirm the zero-dimensional nature of the inorganic substructure: the $[ZnCl_4]^{2-}$ tetrahedra remain fully isolated and evenly distributed, acting as inorganic nodes around which the organic cations and water molecules assemble. The quinolinium cations adopt orientations imposed by the lattice symmetry. Along the *b* axis, their nearly parallel aromatic rings form extended $\pi\cdots\pi$ stacks, while along the *a* and *c* axes they appear tilted or staggered, reducing steric clashes and enabling favorable C–H⋯Cl and C–H⋯π contacts. These controlled orientations illustrate the flexibility of the quinolinium scaffold in establishing complementary electrostatic and π-driven interactions. Water molecules occupy small interstitial sites and serve as efficient hydrogen-bond donors bridging chloride ligands and protonated nitrogen atoms. This O–H⋯Cl/N–H⋯O network consolidates the packing and contributes to the high measured density, indicating a compact structure with minimal unused volume. Symmetry operations propagate these motifs throughout the lattice, producing regular stacks of quinolinium cations interleaved with isolated tetrahedral anions. The layered-like architecture observed along the *c* axis suggests a degree of anisotropy arising from the directional alignment of the π-systems. Overall, the packing arrangement shown in Fig. 2 demonstrates how isolated inorganic clusters, π-stacked organic layers, and a well-positioned hydrogen-bonding network combine to produce a compact, well-organized, and structurally stable hybrid material. This precise arrangement of inorganic and organic domains is a major contributor to the robustness and coherence of $(C_9H_8N)_2[ZnCl_4]\cdot 2H_2O$.

Fig. 3 highlights the coordination polyhedron around the Zn^{2+} center in $(C_9H_8N)_2[ZnCl_4]\cdot 2H_2O$, offering a focused view of

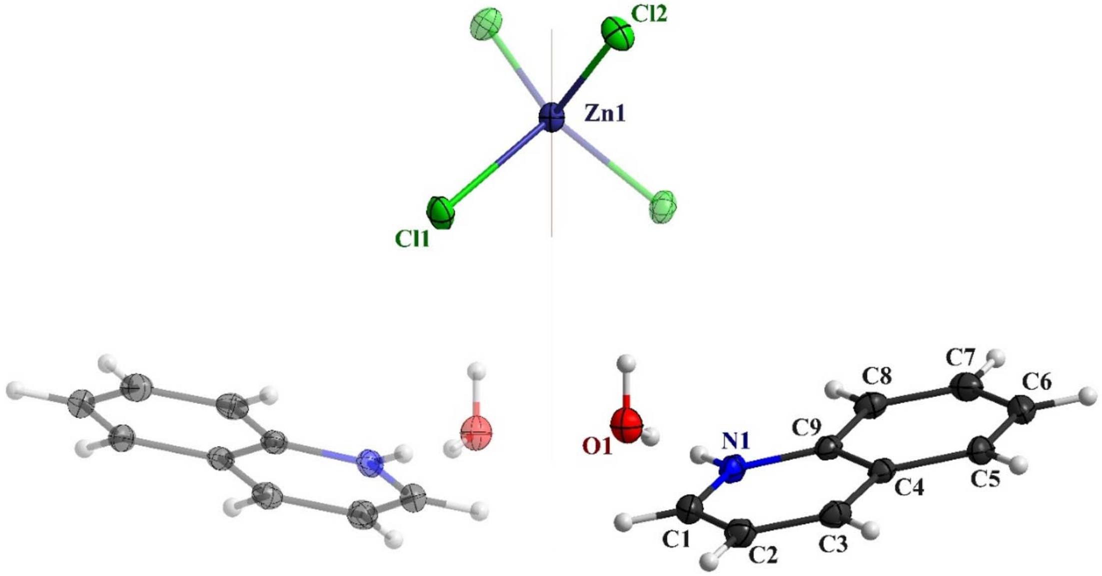

Fig. 1 Asymmetric unit of the titled compound completed by symmetry.

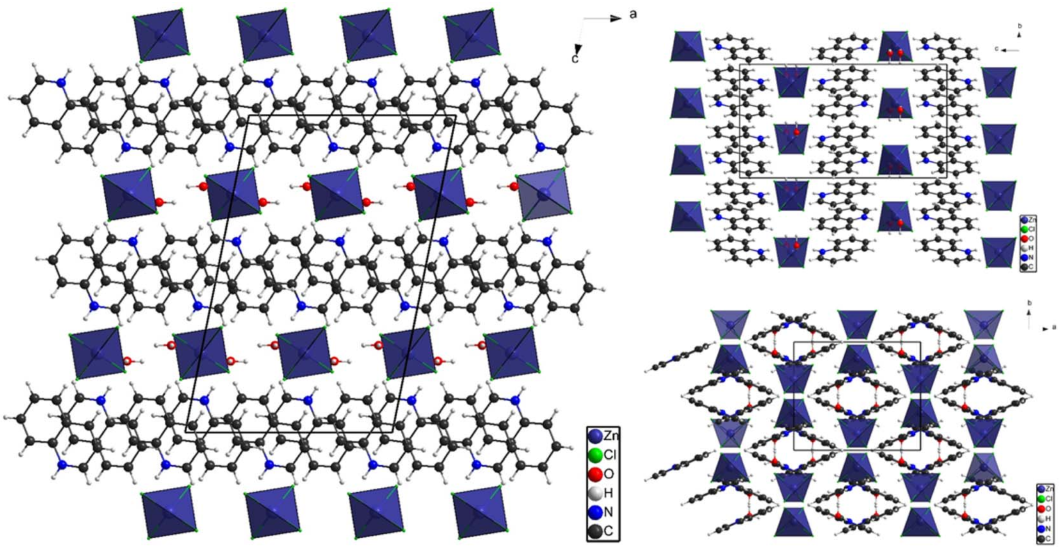

Fig. 2 Crystal packing of $(C_9H_8N)_2[ZnCl_4]\cdot 2H_2O$ along the three principal axes (*a*, *b*, *c*).

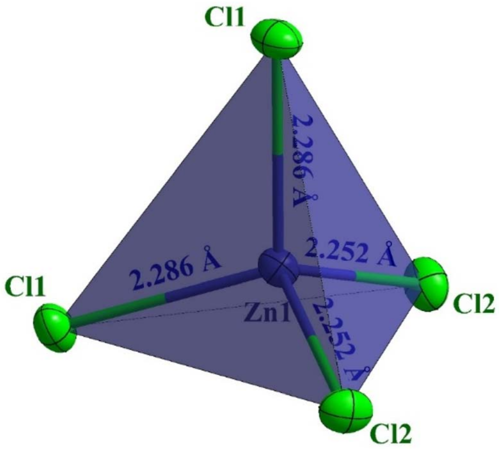

Fig. 3 Distorted tetrahedral coordination environment of Zn^{2+} in the $[ZnCl_4]^{2-}$ anion.

the discrete $[ZnCl_4]^{2-}$ anion and the bond metrics that define its geometry. The zinc atom is tetrahedrally coordinated by four chloride ligands, the most common arrangement for halozincate species. Although an ideal tetrahedron would display uniform Zn–Cl distances and angles of 109.5°, the refined structure shows slight but meaningful deviations—typical of hybrid halometallates where the inorganic fragment responds to its asymmetric environment. These variations reflect the influence of nearby quinolinium cations and hydrogen-bonding water molecules, which impose subtle electrostatic and steric constraints on the coordination sphere. The polyhedral representation reveals that two Zn–Cl bonds are marginally longer than the other two, indicating a modest tetragonal compression. This distortion correlates with the supramolecular role of specific chloride ligands: those involved in stronger Cl⋯H hydrogen bonds with water molecules or C–H groups experience slight weakening of the Zn–Cl bond, whereas the less engaged chlorides retain shorter, stronger interactions. Corresponding angular deviations arise from steric proximity to the organic cations, further contributing to the non-ideal geometry. Despite these irregularities, the overall tetrahedral arrangement remains intact, ensuring the stability of the inorganic fragment within the lattice.

From a structural standpoint, the observed distortions help clarify how the local environment shapes the behavior of the inorganic anion. A near-ideal tetrahedron promotes uniform electron distribution around Zn^{2+}, while minor asymmetry introduces localized differences in bonding strength. These subtle changes may influence properties such as the dielectric environment, vibrational features, and even thermal behavior, where slightly elongated Zn–Cl bonds often act as the first

Table 3 Comparison of structural parameters of selected $[ZnCl_4]^{2-}$-based hybrid compounds

Compound	Organic cation	Zn–Cl bond distances (Å)	$[ZnCl_4]^{2-}$ tetrahedral distortion	Key interactions	Ref.
$(C_9H_8N)_2[ZnCl_4]\cdot 2H_2O$	Quinolinium	2.25–2.29	Slightly distorted	π–π stacking; H-bonding; C–H⋯Cl contacts	This work
$[ZnCl_4]$-pyridinium	Pyridinium	2.25–2.28	Nearly ideal	H-bonding	16
$[ZnCl_4]$-imidazolium	Imidazolium	2.26–2.30	Slightly distorted	H-bonding	17
$[ZnCl_4]$-benzimidazolium	Benzimidazolium	2.25–2.29	Moderately distorted	π–π stacking; H-bonding	16

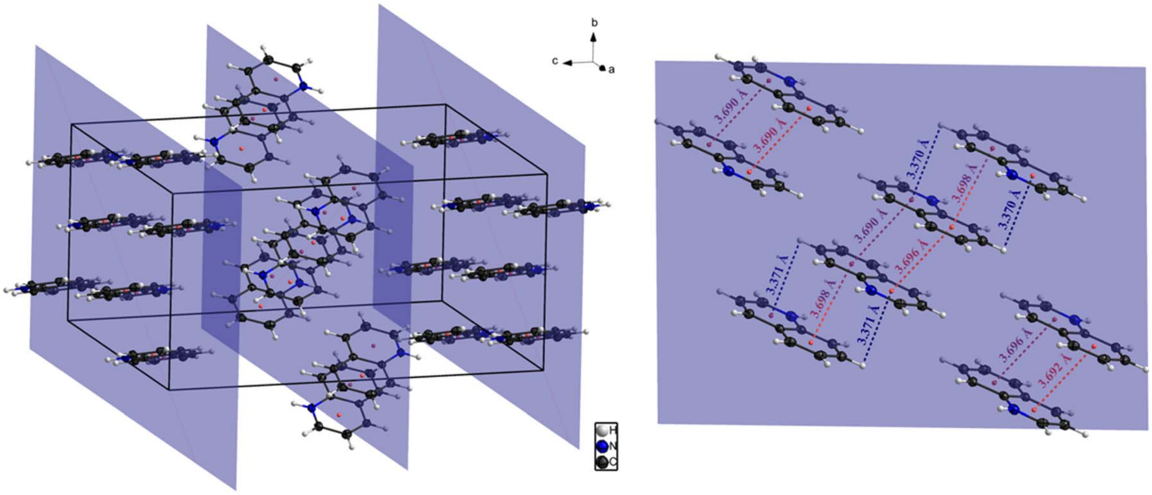

Fig. 4 Different types of π-interactions: red (π⋯π), blue (C–H⋯π).

points of perturbation. The deviations observed in Fig. 3 therefore reflect not disorder, but the fine balance between coordination geometry and supramolecular forces that ultimately governs the stability and reactivity of the hybrid material.

To further assess the structural features and highlight the distinctiveness of the present compound, a comparison with related zinc halometallate hybrids containing nitrogen-based heterocyclic cations was performed. Previously reported systems based on pyridinium, imidazolium, and benzimidazolium cations typically exhibit tetrahedral $[ZnCl_4]^{2-}$ units with Zn–Cl bond distances ranging from approximately 2.25 to 2.30 Å, reflecting varying degrees of distortion depending on the surrounding supramolecular environment.[16,17]

In the title compound, the Zn–Cl bond lengths fall within a comparable range but display slight anisotropy, consistent with the influence of hydrogen bonding and π-interactions involving the quinolinium cations. Compared to simpler heterocyclic cations (Table 3), the quinolinium moiety, with its extended π-conjugated system, promotes stronger π–π stacking and additional intermolecular interactions, which contribute to subtle distortions of the coordination geometry. This behavior is further supported by the observed variation in Zn–Cl bond lengths and bond angles, indicating a deviation from ideal tetrahedral symmetry.

These observations suggest that, while the fundamental $[ZnCl_4]^{2-}$ structural motif remains conserved, the incorporation of quinolinium cations introduces a distinct supramolecular environment that differentiates the present compound from previously reported zinc halometallate hybrids. This comparison supports the structural originality of the system and highlights the role of the organic cation in modulating both local geometry and crystal packing.

The supramolecular organization is further stabilized by π–π stacking interactions between adjacent quinolinium rings (Fig. 4). These interactions are characterized by centroid-to-centroid distances of 3.698 and 3.690 Å, with corresponding interplanar separations of 3.365 and 3.478 Å, respectively. The associated slippage angles of 1.05° and 2.28° indicate a nearly parallel arrangement with slight displacement, typical of efficient aromatic stacking interactions.

In addition, weak C–H⋯π interactions are observed, with a centroid-to-atom distance of 3.370 Å, an interplanar separation of 3.365 Å, and a slippage angle of 1.07°, further contributing to the stabilization of the crystal packing. These interactions, together with the hydrogen-bonding network, lead to a robust three-dimensional supramolecular architecture.

Detailed geometric parameters are provided in the SI (Table S5).

Fig. 5 illustrates how halogen-type and weak intermolecular interactions contribute to the supramolecular architecture of $(C_9H_8N)_2[ZnCl_4]\cdot 2H_2O$, complementing the hydrogen-bonding and π-stacking networks described earlier. The chloride ligands of the $[ZnCl_4]^{2-}$ tetrahedron act not only as coordination partners to Zn^{2+} but also as active acceptors for various noncovalent contacts. Numerous C–H⋯Cl interactions, involving polarized aromatic and aliphatic hydrogens, exhibit favorable geometries that enhance electrostatic complementarity. Although weaker than O–H⋯Cl hydrogen bonds, their multiplicity significantly reinforces the crystal packing, giving chloride ligands a central supramolecular role.

Additional weak interactions provide further stabilization. The electron distribution within the quinolinium rings allows certain C–H groups to interact with chloride ions or π-systems, leading to C–H⋯π contacts that help maintain the slipped π⋯π arrangement and, in some regions, link adjacent layers. These interactions reduce lattice slippage and enhance structural cohesion.

Together, these interactions highlight the multifunctional role of the structural units in this hybrid system. Chloride ligands contribute beyond coordination through hydrogen bonding and electrostatic interactions, while quinolinium cations participate *via* π-stacking and additional weak contacts. This dense network of interactions ensures crystal compactness and contributes to the overall stability. Functionally, such interactions may influence optical and vibrational properties by

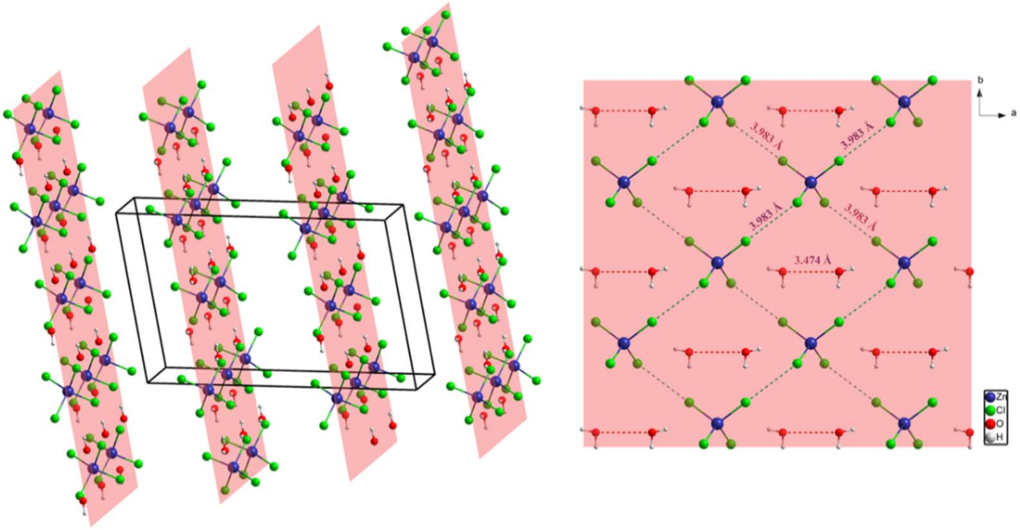

Fig. 5 Halogen and chalcogen interactions in $(C_9H_8N)_2[ZnCl_4]\cdot 2H_2O$.

modulating the local electronic environment around the $[ZnCl_4]^{2-}$ units and may also play a role in intermolecular recognition processes, supporting the multifunctional character of the material.

Fig. 6 depicts the hydrogen-bonding framework of $(C_9H_8N)_2[ZnCl_4]\cdot 2H_2O$, which plays a decisive role in stabilizing the supramolecular architecture of the crystal. The hydrogen-bonding network is constructed from a combination of O–H⋯Cl, N–H⋯O, and weaker secondary contacts, linking together the inorganic tetrahedra, organic cations, and water molecules into a highly cohesive lattice. The crystallographically determined bond metrics confirm the presence of strong and directional interactions, consistent with the compact nature of the structure.

The first set of interactions involves the solvation water molecules acting as donors. In the contact O1–H1B⋯Cl2 [D–H = 0.87 Å, H⋯A = 2.58 Å, D⋯A = 3.283 Å, ∠D–H⋯A = 139°], the geometry reflects a moderately strong hydrogen bond, though the slightly bent angle indicates adaptation to local steric constraints. By contrast, the second water-mediated bond, O1–H1C⋯Cl1 [D–H = 0.87 Å, H⋯A = 2.30 Å, D⋯A = 3.1499(11) Å, ∠D–H⋯A = 165°], is much stronger and nearly linear, representing a highly efficient O–H⋯Cl interaction. Together, these contacts demonstrate that the two symmetry-related water molecules act as bridging nodes within the supramolecular network, simultaneously stabilizing the chloride ligands of different $[ZnCl_4]^{2-}$ tetrahedra and maintaining lattice cohesion.

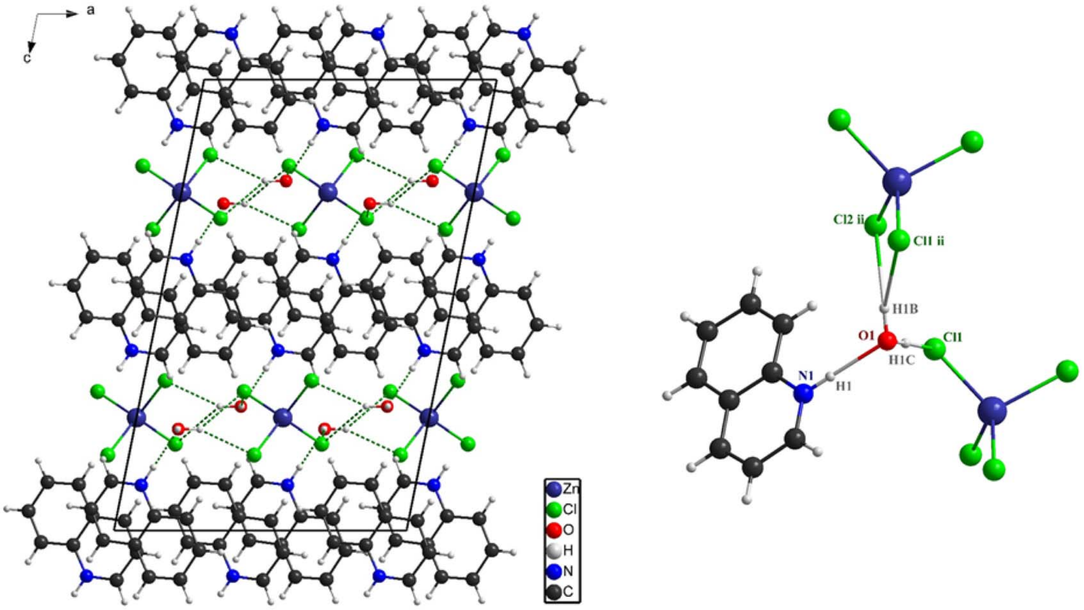

Fig. 6 Hydrogen-bonding framework involving O–H⋯Cl and N–H⋯O interactions.

A particularly striking feature of the hydrogen-bonding scheme is the N1–H1⋯O1 interaction [D–H = 0.88 Å, H⋯A = 1.86 Å, D⋯A = 2.7412(14) Å, ∠D–H⋯A = 179°]. This bond, involving the protonated nitrogen atom of the quinolinium cation and the oxygen atom of the water molecule, is both short and nearly linear, placing it unequivocally in the category of strong hydrogen bonds. Its directionality (179°) implies an optimal donor–acceptor overlap, reinforcing the role of the water molecules as central pillars of the hydrogen-bond network. Functionally, this bond anchors the organic and solvent sublattices together, enabling the propagation of a three-dimensional supramolecular framework that ties the organic cations, inorganic tetrahedra, and solvent molecules into a single cohesive structure.

The combination of these interactions results in a multi-tiered hydrogen-bonding network, where water molecules act as critical bridges, simultaneously linking inorganic and organic components, while the protonated amine groups of quinolinium further consolidate this network through their strong N–H⋯O contacts. The cooperative action of O–H⋯Cl and N–H⋯O bonds imparts significant structural rigidity and minimizes free volume, consistent with the measured crystal density (1.602 Mg m^{-3}). Importantly, this dense hydrogen-bond network is expected to strongly influence the thermal stability of the compound, as hydrogen-bond rupture often represents the first step in dehydration or structural collapse during thermogravimetric analysis. Similarly, hydrogen bonding plays a crucial role in defining the optical properties by modulating local electronic environments around the π-systems, as well as in potential biological interactions, where hydrogen-bond donors and acceptors often determine binding affinity to biomolecular targets.

3.2 Vibrational study

The infrared spectrum of the hybrid zinc–quinolinium salt provides comprehensive information on the bonding motifs that corroborate the single-crystal X-ray diffraction data as shown in Fig. 7. A very broad absorption band between 3485 and 3200 cm^{-1} corresponds to the ν(O–H) stretching vibrations of the two crystallographic water molecules. The remarkable breadth and reduced frequency of this band compared to "free" water are consistent with strong hydrogen bonding, in which the water molecules donate hydrogen atoms to chloride ligands of the $[ZnCl_4]^{2-}$ unit and accept protons from the quinolinium cation. These assignments are supported by the short O–H⋯Cl and N–H⋯O distances observed in the structural refinement, which confirm the hydrogen-bonding network responsible for stabilizing the three-dimensional lattice.[50] A distinct sharp band at 3195 cm^{-1} is ascribed to ν(N–H) stretching of the protonated quinolinium group. The downshift relative to neutral quinoline arises from protonation at the heteroaromatic nitrogen atom, a feature also reflected in the strong N–H⋯O water hydrogen bond revealed by crystallography. Weak absorptions between 3087 and 3038 cm^{-1} correspond to aromatic ν(C–H) stretches of the quinolinium ring, while aliphatic C–H modes are observed in the 2950–2850 cm^{-1} region, typical of substituted aromatic systems. A prominent band at 1620 cm^{-1} is assigned to the ν(C═N) stretching vibration of protonated quinolinium. Its significant red-shift compared with neutral quinoline derivatives reflects both the positive charge delocalization and the π–π stacking interactions revealed along the crystallographic *b* axis, which reduce electron density on the imine group. Additional absorptions in the 1570–1500 cm^{-1} and 1450 cm^{-1} regions are attributed to aromatic ν(C═C) skeletal modes, while the 1250–1220 cm^{-1} region is dominated by ν(C–N) stretching. Finally, the far-infrared spectrum reveals multiple absorptions between 500 and 300 cm^{-1}, corresponding to Zn–Cl stretching vibrations of the tetrahedral $[ZnCl_4]^{2-}$ anion. The observed splitting of these bands matches the slight distortion of the tetrahedron (two Zn–Cl bonds elongated to 2.285 Å compared to 2.252 Å for the others), as asymmetry lifts vibrational degeneracy and produces the series of distinct absorptions.[24,51]

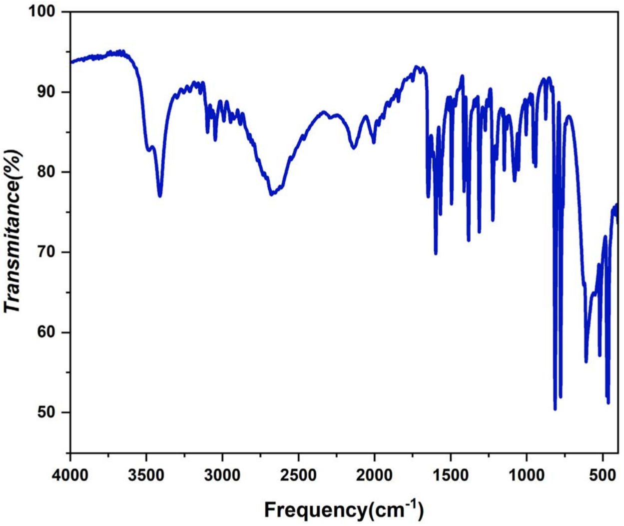

Fig. 7 The infrared spectrum of $(C_9H_8N)_2[ZnCl_4]\cdot 2H_2O$.

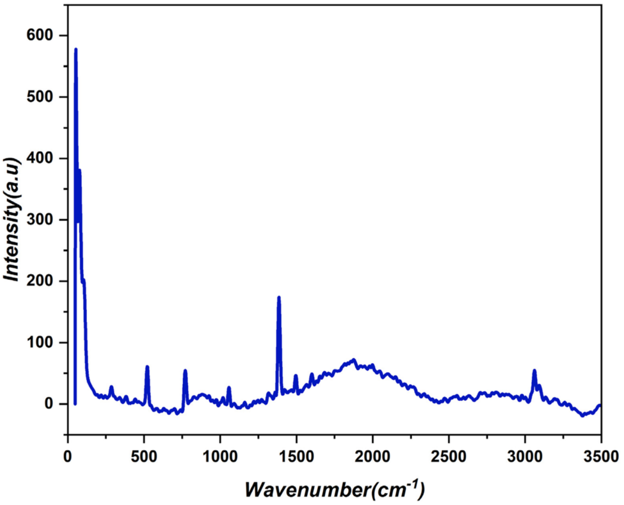

Fig. 8 The Raman spectrum of the complex $(C_9H_8N)_2[ZnCl_4]\cdot 2H_2O$.

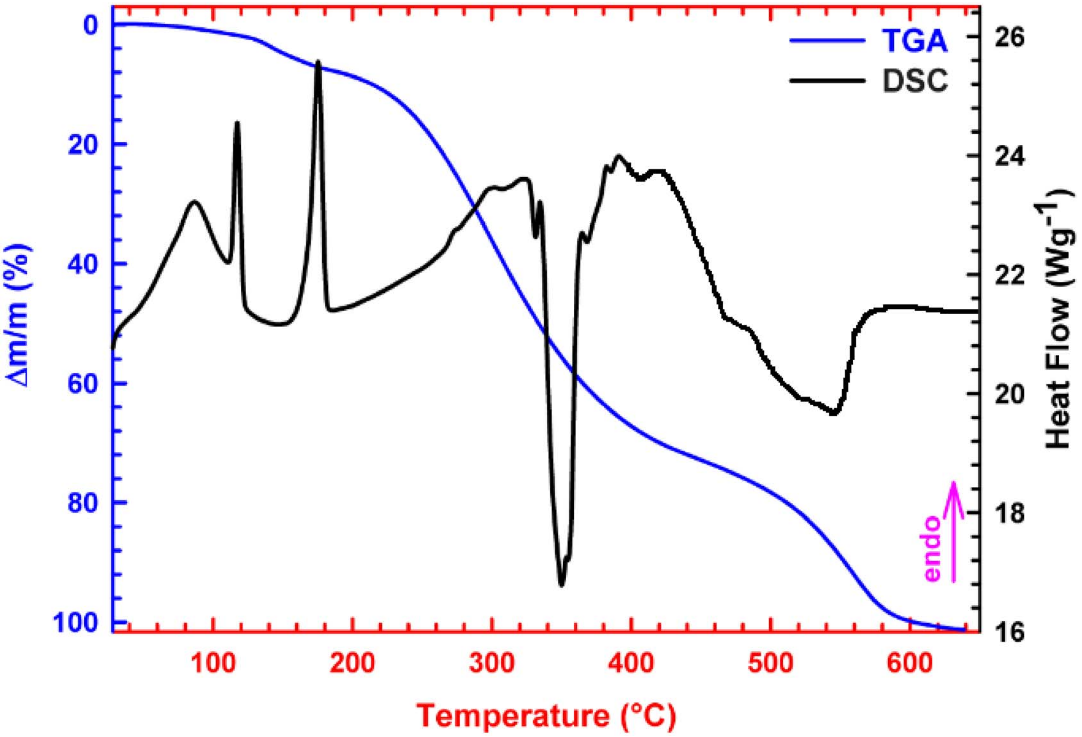

Fig. 9 The TGA-DSC curves of $(C_9H_8N)_2[ZnCl_4]\cdot 2H_2O$.

The Raman spectrum (Fig. 8) of the same material complements the IR findings and highlights vibrational features that are either weak or silent in IR spectroscopy. A well-defined peak at 1648 cm^{-1} is attributed to the δ(H–O–H) bending vibration of the lattice water molecules. This assignment is consistent with the bending frequency of strongly hydrogen-bonded water reported in crystalline hydrates, and its intensity reflects the directional O–H⋯Cl and O–H⋯N interactions described in the structural analysis.[52] The aromatic region of the Raman spectrum displays a strong peak at 1600 cm^{-1}, assigned to the ν(C=N) stretch of protonated quinolinium. The band is polarized and enhanced in intensity, in agreement with the increased polarizability of the protonated heteroaromatic ring. Two additional peaks at 1491 and 1382 cm^{-1} correspond to ν(C=C) and in-plane ν(C–N) stretching modes, respectively. Their positions and intensities are typical for quinolinium salts and confirm the protonation-induced changes in the electronic distribution of the cation.[53] The low-frequency Raman region provides the clearest evidence for the internal modes of the $[ZnCl_4]^{2-}$ tetrahedron. Distinct bands at 347, 310, 248, and 114 cm^{-1} can be assigned to the ν_3 (F_2, asymmetric stretch), ν_1 (A_1, symmetric stretch), ν_4 (F_2, asymmetric bend), and ν_2 (E, symmetric bend) vibrational modes, respectively. Additional lattice modes are detected below 100 cm^{-1}, corresponding to external translational and librational motions of the tetrahedral anions within the hydrogen-bonded network. Compared with ideal Td symmetry, the splitting and frequency shifts observed here are direct vibrational fingerprints of the small but significant Zn–Cl bond length inequalities measured crystallographically. Such distortions are known to perturb the vibrational degeneracy of halozincate tetrahedra, and similar effects have been reported in other tetrahalometallate salts studied by polarized Raman spectroscopy.[54,55] The excellent agreement between the structural and vibrational data confirms that the combined IR and Raman analyses provide a complete picture of the bonding environment and subtle distortions present in this zinc-based hybrid, the assignments are presented in Table S6.

3.3 Thermal behavior

The thermal behavior of $(C_9H_8N)_2[ZnCl_4]\cdot 2H_2O$ was investigated by coupled DSC–TGA analysis under an oxygen atmosphere (Fig. 9), revealing a multistep decomposition pathway. An initial endothermic event below 200 °C, accompanied by a mass loss of 6.6%, corresponds to the release of two lattice water molecules (calcd ≈ 6.5%), confirming the dehydration process. The anhydrous phase remains stable up to ∼250 °C, where a pronounced thermal event is observed, consistent with the onset of melting and structural destabilization. A major mass loss of 65.5% occurs between 250 and 450 °C, associated with the decomposition of quinolinium cations and the breakdown of the $[ZnCl_4]^{2-}$ anion, leading predominantly to the evolution of HCl and volatile organic species. At higher temperatures (450–600 °C), a further loss of 26.6% is observed, which is mainly attributed to the volatilization of $ZnCl_2$, with possible minor formation of ZnO due to residual oxygen or moisture. The absence of a stable residue at the end of the experiment supports the volatilization-driven decomposition mechanism. Overall, the DSC and TGA results are fully consistent and indicate a sequential process involving dehydration, melting, organic framework collapse, and final inorganic volatilization.[56–58]

3.4 UV-vis-NIR diffuse reflectance spectroscopy

To probe the optical response of the material in the solid state, the diffuse reflectance spectrum was converted into the absorption-like Kubelka–Munk function F(R), allowing direct visualization of the electronic transitions. The diffuse-reflectance-derived absorption profile of $(C_9H_8N)_2[ZnCl_4]\cdot 2H_2O$, expressed through the Kubelka–Munk function F(R) (Fig. 10), reveals three well-defined electronic transitions that reflect both the organic–inorganic duality of the hybrid lattice and the specific electronic structure imposed by the $ZnCl_4^{2-}$ coordination environment. The high-energy band at 235 nm is characteristic of $\pi \rightarrow \pi^*$ excitations within the aromatic cationic sublattice, consistent with the conjugated framework of the $C_9H_8N^+$ units. A second feature centered around 315 nm is attributed to an interband excitation involving localized electronic states within the hybrid solid, most plausibly an electron–hole–type transition associated with shallow sub-gap states that arise from the electronic coupling between the organic moieties and the tetrahalozincate unit. Unlike molecular $n \rightarrow \pi^*$ processes, which are typically weaker, this transition presents as a broader, more solid-state-like excitation, coherent with the extended lattice environment. The lower-energy band at 350 nm is assigned to a ligand-to-metal charge-transfer (LMCT) process of the type $Cl^- \rightarrow Zn^{2+}$, a well-documented feature in d^{10} zinc–halide complexes. The absence of any d–d transitions, expected for Zn^{2+} ($3d^{10}$, filled), further confirms that the optical activity stems from organic π-systems, solid-state interband processes, and LMCT transitions rather than from intra-metal excitations.

The band-gap characteristics of $(C_9H_8N)_2[ZnCl_4]\cdot 2H_2O$ were examined using the modified Tauc approach presented in Fig. 11, in which F(R), derived from diffuse reflectance *via* Kubelka–Munk transformation, substitutes for the absorption coefficient (Fig. 10). The Kubelka–Munk theory, commonly applied to analyze DRS data from weakly absorbing powders, was used to refine the band gap estimation. The Kubelka–Munk function, defined as:[59,60]

$$\mathrm{F(R)} = \frac{K}{S} = \frac{(1 - R_\infty)^2}{2R_\infty}$$

In this context, R represents the absolute reflectance of the sample, measured using an integrating sphere system. K is the light absorption coefficient, and S is the scattering coefficient. The function (R) is known as the Kubelka–Munk function. According to inter-band absorption theory, the absorption coefficient near the threshold, in relation to incident energy, can be described by the following equation:[60,61]

$$\left[\frac{\mathrm{F(R)}h\nu}{t}\right]^{\frac{1}{n}} = A\left(h\nu - E_g\right)$$

In the energy interval of 3.5–4.0 eV, both the direct and indirect Tauc representations exhibit linear regions associated with the onset of the high-energy excitation identified in the F(R) spectrum. However, distinction between the two possible transition types was achieved through the analysis of the slope-exponent method, based on the $\ln(\mathrm{F(R)}\cdot h\nu)$ *versus* $\ln(h\nu)$ plot. The extracted exponent $n \approx 2$ indicates an indirect allowed transition, consistent with the expected electronic structure of $ZnCl_4^{2-}$-based hybrid frameworks, where lattice–orbital interactions typically promote indirect optical processes. Consequently, the indirect Tauc fit was used to determine the optical band gap, yielding $E_g = 3.02$ eV. This value falls within the range characteristic of wide-band-gap semiconductors. The absorption-edge estimate at 373 nm corresponds to an energy of approximately 3.32 eV, slightly higher than the Tauc-derived value due to the inherent difference between edge-based and linear extrapolation methods. Together, the Tauc behavior and the n-value analysis confirm that the compound is an indirect-gap semiconductor with a well-defined band-edge transition.

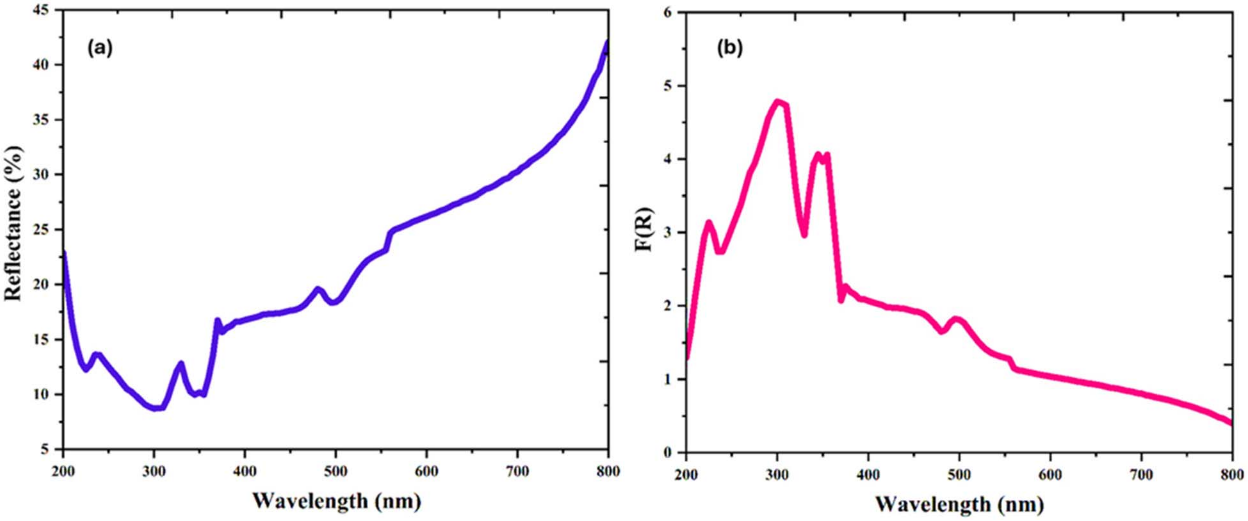

Fig. 10 (a) Diffuse reflectance spectrum of the $ZnCl_4$-based hybrid material transformed using the Kubelka–Munk function F(R); (b) corresponding absorption profile highlighting the main electronic transitions.

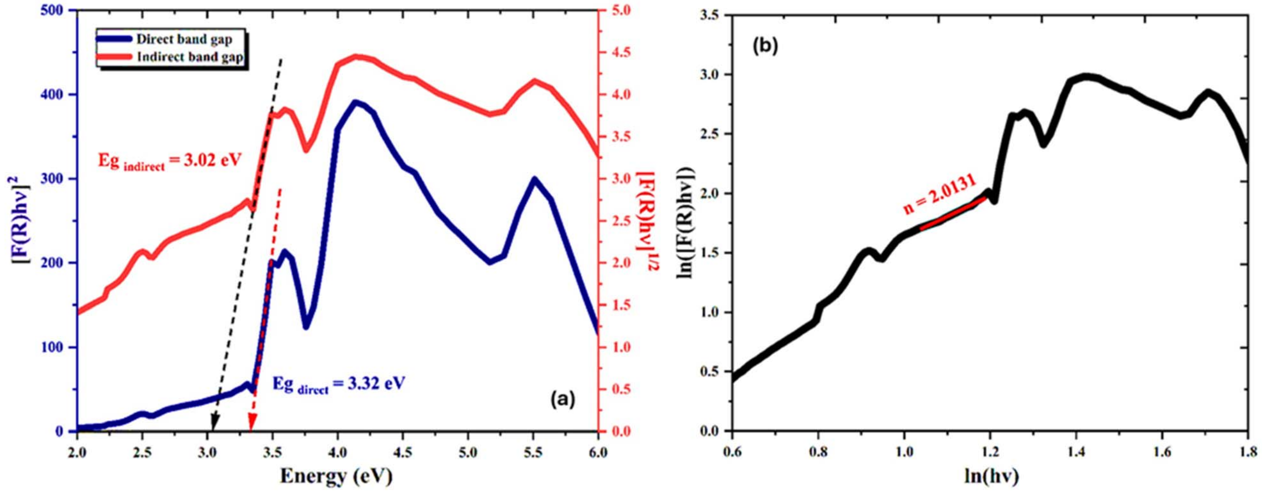

Fig. 11 (a) Tauc plot for direct allowed electronic transitions derived from Kubelka–Munk–transformed diffuse reflectance data; (b) linear extrapolation used for determination of the optical band gap.

Further insight into the electronic disorder and sub-band-gap absorption processes in $(C_9H_8N)_2[ZnCl_4]\cdot 2H_2O$ was obtained through an analysis of the Urbach tail, which reflects the exponential absorption behavior near the optical edge (Fig. 12).

The formula used is:

$$\ln(\alpha) = \ln(\alpha_0) + \frac{h\nu}{E_u}$$

where α is the absorption coefficient, $h\nu$ the photon energy, and E_u the Urbach energy.

Using the Kubelka–Munk-derived quantity F(R), the low-energy region below 3.5 eV was fitted according to the Urbach model, wherein the absorption tail follows an exponential dependence governed by the Urbach energy, E_u. This region of the spectrum captures the transition from the steep absorption onset to the more diffuse tail arising from lattice fluctuations, microstructural disorder, and the inherent dynamic flexibility of hybrid organic–inorganic frameworks. The fit to the exponential regime yielded an Urbach energy of 0.212 eV, indicative of a moderately broad tail. Such an E_u value reflects the presence of localized states within the forbidden gap, which commonly originate from structural disorder associated with hydrogen-bonding variability in the organic layers, slight distortions within the $ZnCl_4{}^{2-}$ tetrahedra, or vibrational coupling between organic and inorganic subunits. When expressed as a fraction of the optical band gap (E_u/E_g), the Urbach width represents approximately 7.02% of the total band-gap energy. This proportion is consistent with hybrid systems where static and dynamic disorder coexist due to the soft lattice nature introduced by the organic moieties and the polarizable halide coordination sphere. The comparatively pronounced magnitude of E_u also aligns with the indirect band structure determined from the Tauc analysis, as indirect-gap semiconductors frequently exhibit stronger phonon–electron

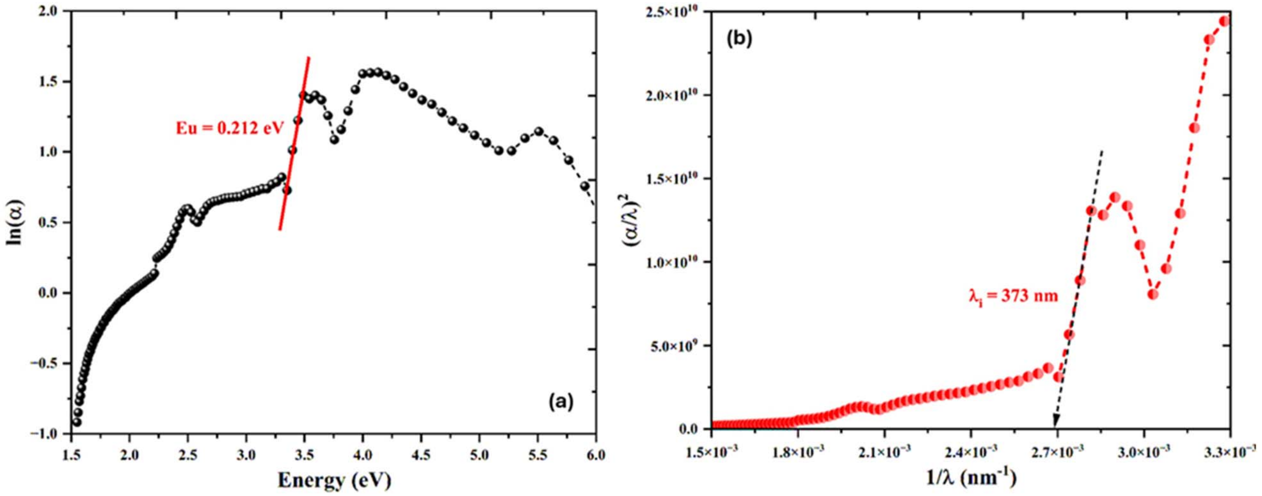

Fig. 12 (a) Urbach plot illustrating the exponential absorption edge of the $ZnCl_4$-based hybrid material; (b) linear fitting used to extract the Urbach energy.

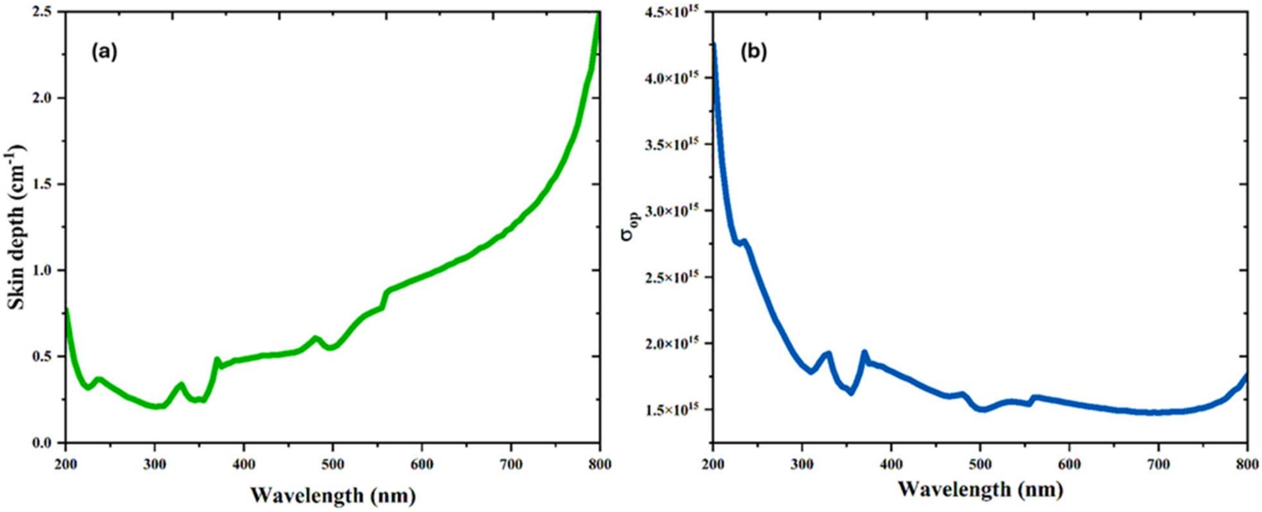

Fig. 13 (a) Photon-energy-dependent optical conductivity of the $ZnCl_4$-based hybrid material; (b) corresponding variation of the skin depth as a function of photon energy.

coupling, contributing to a more extended exponential absorption tail.

Overall, the Urbach analysis underscores the role of lattice disorder, excitonic effects, and local structural fluctuations in shaping the sub-gap optical response of this $ZnCl_4$-based organic–inorganic system, providing a complementary perspective to the band-edge behavior outlined in the Tauc-derived band gap.

To further elucidate the charge-transport-related optical properties of $(C_9H_8N)_2[ZnCl_4]\cdot 2H_2O$, the frequency-dependent optical conductivity $\sigma(\omega)$ and the corresponding skin depth $\delta(\omega)$ were evaluated from the Kubelka–Munk–derived optical functions (Fig. 13). It was calculated using the relation:

$$\sigma_{op} = \frac{\alpha(\lambda)n(\lambda)c}{4\pi k(\lambda)}$$

where α is the absorption coefficient, n the refractive index, k the extinction coefficient, and c the speed of light in vacuum these two quantities provide complementary information: while $\sigma(\omega)$ probes the ability of photogenerated carriers to respond to an oscillating electromagnetic field, $\delta(\omega)$ describes how deeply electromagnetic radiation penetrates before being significantly attenuated. Together, they offer a more dynamic perspective on carrier mobility, dielectric screening, and the interaction between the incident light field and the electronic structure of the hybrid lattice. The optical conductivity $\sigma(\omega)$ exhibits a gradual rise across the visible-UV region, with a pronounced increase as the photon energy approaches the band-edge transition identified previously in the Tauc analysis. This behavior is characteristic of wide-band-gap hybrid semiconductors in which conductivity remains low at low energies due to the absence of free carriers, but increases sharply once sufficient energy is available to promote electrons across the gap and into extended states. The onset of enhanced $\sigma(\omega)$ near the band-edge suggests the activation of interband transitions and the initiation of photocarrier generation within the $ZnCl_4^{2-}$ framework, accompanied by contributions from the organic cation layers as excitations couple into higher-energy conduction pathways. The profile of $\sigma(\omega)$ is consistent with the indirect-gap nature of the material, where phonon involvement facilitates carrier excitation and subtly modulates the spectral dependence of the conductivity.

The corresponding skin-depth function $\delta(\omega)$, which quantifies the penetration depth of incident light, reveals a complementary trend. It is given by:[62]

$$\delta(\lambda) = \frac{1}{\alpha(\lambda)}$$

In the low-energy region, $\delta(\omega)$ maintains relatively large values, indicating that the material is highly transparent to lower-energy photons due to minimal interband absorption and low conductivity. As photon energy increases toward the band edge, $\delta(\omega)$ decreases progressively, illustrating the increased attenuation associated with heightened absorption and more effective photocarrier generation. This inverse correlation between $\sigma(\omega)$ and $\delta(\omega)$ is typical of insulating or semi-insulating hybrid materials where dielectric response dominates at low energies and electronic absorption takes over as the band gap is approached. The observed depth variations also highlight the interplay between the organic sublattice—characterized by relatively soft bonding and low electronic density—and the more rigid inorganic $ZnCl_4^{2-}$ moieties that dominate the high-energy optical processes.

Together, the optical conductivity and skin-depth analyses provide a dynamic interpretation of carrier excitation and light–matter interaction within this chlorozincate hybrid. They reinforce the picture of a wide-band-gap, indirect semiconductor with modest low-energy conductivity, strong high-energy absorption, and lattice-coupled photophysical behavior that reflects the dual organic–inorganic nature of the structure.

The dispersion behavior of the extinction coefficient k and the refractive index n provides deeper insight into how

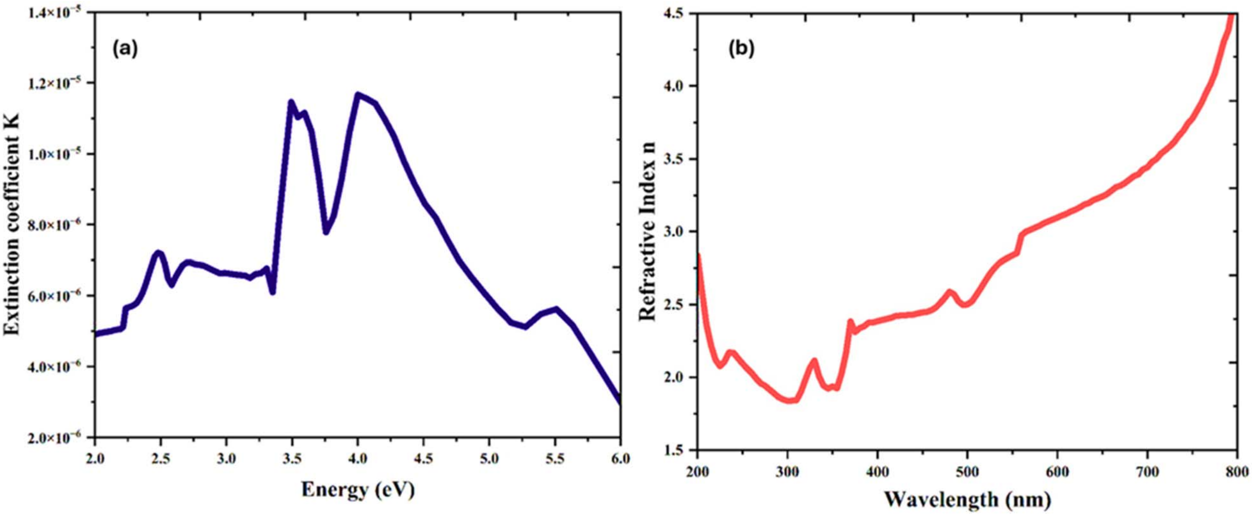

Fig. 14 (a) Dispersion of the refractive index as a function of photon energy; (b) corresponding extinction coefficient illustrating absorption behavior near the band edge.

$(C_9H_8N)_2[ZnCl_4]\cdot 2H_2O$ interacts with electromagnetic radiation across the UV-visible range (Fig. 14). These two optical constants, derived from the Kubelka–Munk–based formalism and the associated reflectance transformations, are essential for understanding both the absorptive and dispersive characteristics of the material. Their combined behavior reflects the interplay between electronic transitions, dielectric response, and the structural duality inherent to organic–inorganic hybrid halometallates.

The optical extinction coefficient (λ) describes the combined effect of absorption and scattering of light within the material, providing direct insight into its electronic transitions, and is expressed as:[63]

$$K(\lambda) = \frac{\lambda \alpha(\lambda)}{4\pi}$$

The extinction coefficient k displays a characteristic low baseline at lower energies, consistent with negligible absorption far below the band edge and confirming the high optical transparency of the compound in the visible region. As the photon energy increases and approaches the electronic transition thresholds identified in the F(R) spectrum, k rises sharply, marking the onset of strong attenuation due to interband excitations. This increase traces the cumulative effect of $\pi \rightarrow \pi^*$, shallow electronic–state transitions, and LMCT processes involving the $ZnCl_4^{2-}$ coordination sphere. The profile of k is typical of wide-band-gap inorganic–organic materials, where absorption remains minimal until the vicinity of the primary photoactive transitions and then escalates rapidly due to a high density of accessible conduction-band states.

The refractive index (n) quantifies the interaction between incident light and the material's electronic structure, reflecting its polarizability and optical density. It was computed using the following relation:[64]

$$n(\lambda) = \frac{1 + R + \sqrt{4R - (1 - R)^2 K^2}}{1 - R} = \frac{1 + R}{1 - R} + \sqrt{\frac{4R}{(1 - R)^2} - K^2}$$

In parallel, the refractive index n reveals a dispersion pattern that reflects both electronic polarizability and the hybrid lattice's structural characteristics. At low energies, n attains relatively elevated values, a behavior often observed in polarizable halometallate systems where the heavy atoms (such as Cl^- and Zn^{2+}) and the organic cations collectively contribute to a strong dielectric response. As photon energy increases, n follows a normal dispersion trend, gradually decreasing across the visible range before undergoing more pronounced variation near the absorption edge. This normal-to-anomalous dispersion transition corresponds to the proximity of electronic resonances and is consistent with the material's indirect band-gap nature, where vibrational and lattice interactions modulate the refractive response. Such dispersion characteristics highlight the tendency of hybrid structures to combine the polarizability of organic layers with the more rigid, electronically dense nature of inorganic tetrahalide units.

Taken together, the extinction coefficient and refractive index trends reaffirm the semiconductor-like optical behavior of the hybrid. The evolution of k delineates the threshold of significant photon absorption and electronic activation, whereas n captures the broader dielectric response and dispersive dynamics of the lattice. Their combined analysis underscores the dual contribution of organic and inorganic components in shaping the optical constants of this $ZnCl_4$-based hybrid material, offering useful parameters for applications in optical modeling, waveguiding design, and photonic materials engineering.

3.5 Computational study

Density Functional Theory (DFT) calculations were employed to evaluate the electron density distribution, frontier molecular

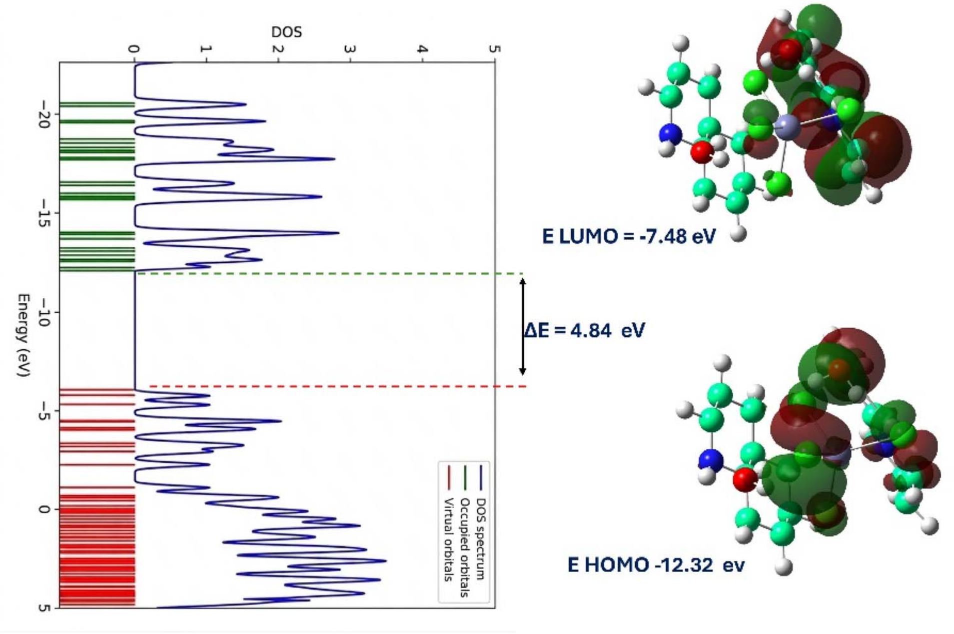

Fig. 15 The DOS Spectrum for the zinc complex.

orbitals, and surface properties of the studied compounds. The SwissTargetPrediction tool was used to identify the most probable biological targets based on the structural features of the compounds. In addition, the BOILED-Egg model was applied to assess gastrointestinal absorption and blood–brain barrier (BBB) permeability of the ligands and their complexes, providing insight into their passive transport behavior. Pharmacokinetic properties were further evaluated using the pkCSM web server. The predicted parameters included water solubility (log mol L^{-1}), Caco-2 permeability ($\log P_{\text{app}}$ in 10^{-6} cm s^{-1}), intestinal absorption (%), skin permeability ($\log K_{\text{p}}$), and P-glycoprotein (P-gp) interactions, including substrate behavior and inhibitory effects on P-gp I and P-gp II. Finally, molecular docking studies were investigated to examine the binding interactions of the $(C_9H_8N)_2[ZnCl_4]\cdot 2H_2O$ complex with key bacterial targets, namely DNA Gyrase and LasR.

3.5.1 DFT and energy analysis of the zinc complex. DFT calculations were performed to elucidate the electronic properties of the Zn complex. The optimized structure exhibits a large negative SCF energy (−4801.86 eV), confirming its high stability. The HOMO and LUMO energies are −12.32 eV and −7.48 eV (Fig. 15), respectively, giving an energy gap of 4.84 eV, indicative of moderate reactivity and good kinetic stability. Experimentally, diffuse reflectance spectroscopy reveals an indirect optical band gap of 3.02 eV, suggesting semiconducting behavior. The lower experimental gap compared to the calculated value is attributed to solid-state and excitonic effects.

The calculated global reactivity descriptors ($\mu = -9.90$ eV, $\eta = 2.42$ eV, $S = 0.207$ eV^{-1}, $\omega = 20.25$ eV) indicate moderate chemical reactivity and electron-accepting ability. Additionally, the high dipole moment (10.45 D) reflects significant molecular polarity (Table S.7). Overall, the Zn complex exhibits a stable electronic structure with semiconducting characteristics and potential for optoelectronic applications.

3.5.2 Estimation of biological availability. The molecular behavior of Ciprofloxacin and the zinc complex $(C_9H_8N)_2[ZnCl_4]\cdot 2H_2O$ was evaluated using SwissADME predictions (Table S.8 and Fig. 16). Ciprofloxacin exhibited a molecular weight (MW) of 331.34 g mol^{-1} and a TPSA of 74.57 Å^2, consistent with favorable drug-like characteristics. In contrast, the zinc complex showed a higher MW (503.56 g mol^{-1}) and a reduced TPSA (46.74 Å^2), reflecting its distinct coordination structure.

Both compounds displayed a marked difference in lipophilicity and aqueous solubility. Ciprofloxacin showed moderate lipophilicity (Consensus $\log P = 1.10$) and high-water solubility, whereas the zinc complex exhibited significantly higher lipophilicity ($\log P = 3.46$) and poor aqueous solubility ($\log S = -7.26$). This indicates a shift toward membrane affinity for the complex, accompanied by reduced solubility in biological media.

Pharmacokinetic (PK) predictions indicated high gastrointestinal (GI) absorption for both compounds, while neither was expected to permeate the blood–brain barrier (BBB), suggesting limited central nervous system exposure. Additionally, both compounds were predicted to be P-glycoprotein (P-gp) substrates, implying potential efflux-mediated reduction in intracellular accumulation.

In terms of drug-likeness, Ciprofloxacin fully complied with Lipinski's and Veber's rules,[65,66] whereas the zinc complex showed one Lipinski violation due to MW > 500 g mol^{-1}, although it retained an acceptable bioavailability score (0.55). Synthetic accessibility (SA) analysis indicated that both compounds are readily synthesizable, with slightly easier synthesis predicted for the zinc complex (SA = 2.23 *vs.* 2.51).

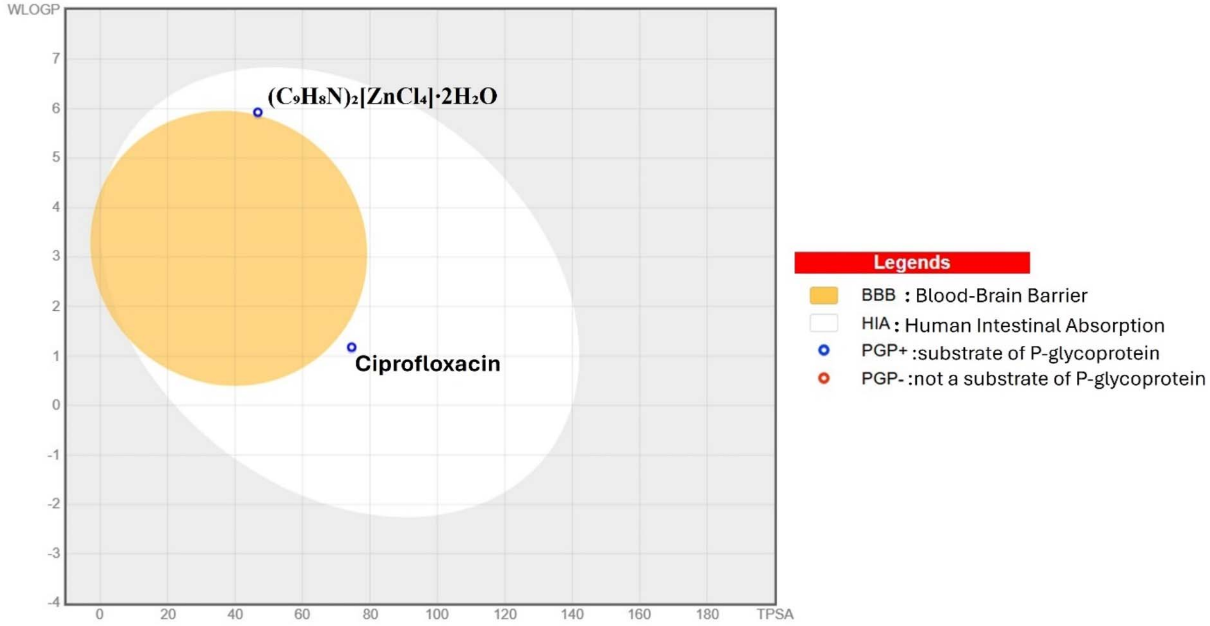

Fig. 16 BOILED-Egg model predictions for Ciprofloxacin and zinc complex.

Overall, the zinc complex $(C_9H_8N)_2[ZnCl_4]\cdot 2H_2O$ demonstrates a distinct physicochemical profile compared to Ciprofloxacin, characterized by increased lipophilicity and reduced solubility while maintaining acceptable oral bioavailability.

3.5.3 Pharmacokinetic properties. From pkCSM-pharmacokinetics,[67] the zinc complex $(C_9H_8N)_2[ZnCl_4]\cdot 2H_2O$ was predicted to exhibit favorable absorption-related pharmacokinetic properties (Table S.7). It shows high Caco-2 permeability ($\log P_{app} = 0.623$) and excellent intestinal absorption (91.6%), indicating efficient gastrointestinal uptake. In contrast, the compound demonstrates moderate aqueous solubility ($\log S = -3.774$) and low skin permeability ($\log K_p = -2.704$), suggesting limited dermal absorption.

Importantly, the zinc complex is not a substrate of P-glycoprotein (P-gp−), but is predicted to act as a P-gp inhibitor (P-gp I and II positive), which may enhance intracellular retention and reduce efflux-mediated drug transport. The results indicate that the zinc complex possesses strong oral

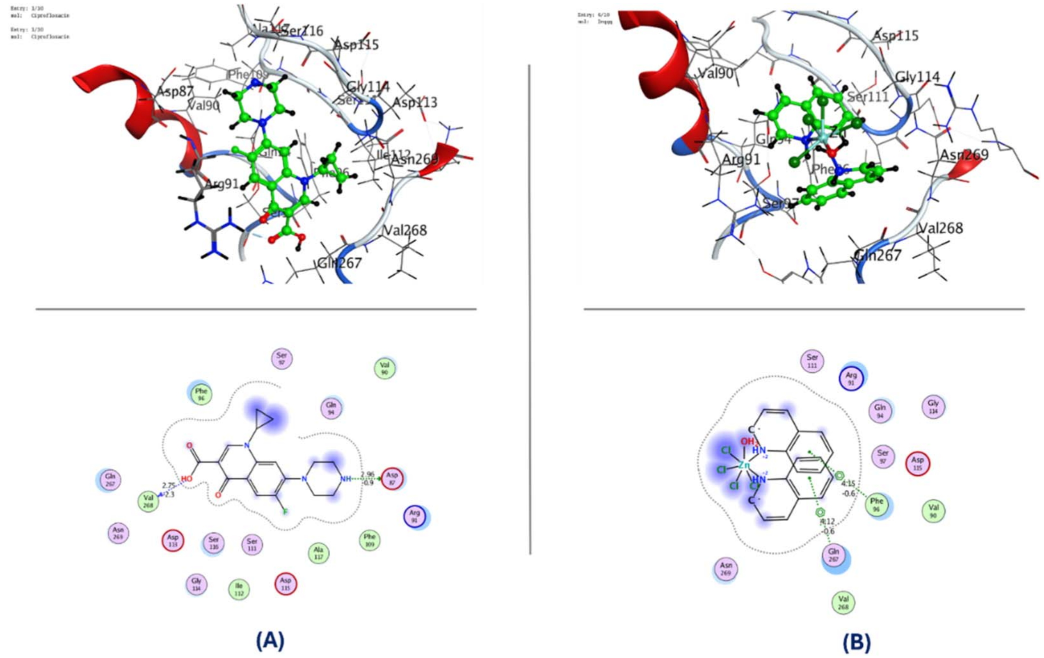

Fig. 17 2D, 3D for Molecular docking of (A) Ciprofloxacin and (B) Zn complex with DNA Gyrase (PDB ID: 1AB4).

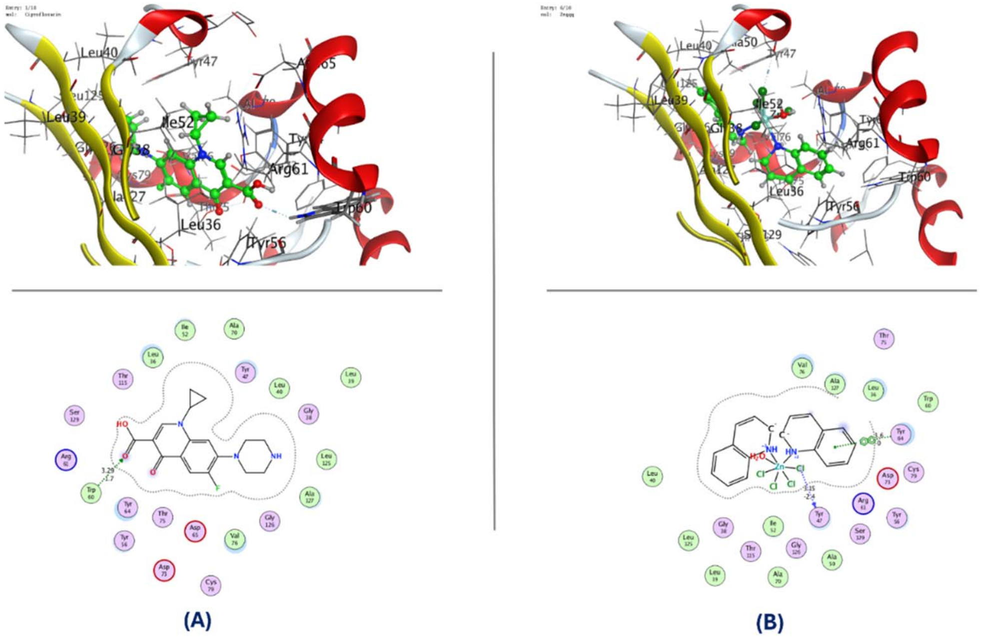

Fig. 18 2D, 3D for Molecular docking of (A) Ciprofloxacin and (B) Zn complex with LasR (PDB ID: 3IX3).

absorption potential with favorable permeability characteristics, despite moderate solubility, and may benefit from reduced P-gp-mediated efflux compared to typical substrates.

3.5.4 Molecular docking. Molecular docking investigations were conducted to elucidate the binding behaviour of ciprofloxacin and the synthesized Zn complex toward DNA gyrase and LasR proteins (PDB IDs: 1AB4 and 3IX3, respectively) (Tables S8, 9, Fig. 17 and 18). The study provides mechanistic insight into ligand–protein recognition, binding energetics, and active-site complementarity. Zinc–quinolone complexes have been widely reported to exhibit enhanced biological activity compared to their free ligands, an effect commonly attributed to chelation-induced lipophilicity and improved membrane permeability. Coordination to Zn(II) is also known to modify electronic distribution and increase molecular rigidity, which can significantly influence ligand–protein interactions in docking studies.[68–70]

Against DNA gyrase (1AB4), ciprofloxacin exhibited a more favourable binding affinity (-6.13 kcal mol^{-1}) than the Zn complex (-4.96 kcal mol^{-1}). The enhanced stability of ciprofloxacin arises from the formation of two key hydrogen-bonding interactions with ASP87 and VAL268, which anchor the ligand within the catalytic pocket and reinforce complex stabilization. In contrast, the Zn complex is predominantly stabilized through weaker π–H contacts with PHE96 and GLN267, indicating limited directional interactions and reduced binding efficiency.

A consistent trend was observed for LasR (3IX3), where ciprofloxacin again demonstrated superior binding affinity (-7.68 kcal mol^{-1}) relative to the Zn complex (-5.88 kcal mol^{-1}). The interaction profile of ciprofloxacin is dominated by a decisive hydrogen bond with TRP60, a residue implicated in ligand recognition within the LasR binding cavity. Conversely, the Zn complex exhibits a mixed interaction landscape involving hydrogen bonding with TYR47 and π⋯π stacking with TYR64; however, these interactions are less effective in achieving optimal stabilization within the hydrophobic pocket.

Collectively, the docking outcomes indicate that ciprofloxacin possesses a more efficient binding mode toward both targets, driven by a well-defined hydrogen-bonding network and superior steric complementarity. In contrast, coordination to Zn(II) introduces increased molecular rigidity and alters electronic distribution, thereby limiting conformational adaptability and attenuating binding efficiency within the protein active sites.

3.6 Antibacterial activity

The antibacterial activity of the $(C_9H_8N)_2[ZnCl_4]\cdot 2H_2O$ compound was evaluated against both Gram-positive and Gram-negative bacterial strains, revealing a pronounced broad-spectrum effect. The compound exhibited a minimum inhibitory concentration (MIC) of 5 μg mL^{-1} for all tested strains, except for *Enterococcus faecalis*, which showed a slightly higher MIC value of 10 μg mL^{-1}. In all cases, the MBC/MIC ratios were lower than 4, confirming the bactericidal nature of the compound.[46,47]

The observed antibacterial activity can be attributed to the effect of metal–ligand complexation. Coordination of the organic ligand to Zn(II) enhances lipophilicity, facilitating membrane permeability and promoting interactions with intracellular targets such as proteins and DNA.[71] This behavior is consistent with previous studies reporting enhanced biological activity of zinc complexes compared to their corresponding free ligands.

Moreover, zinc complexes containing chloride ligands have been shown to exhibit significant antibacterial properties, highlighting the combined influence of the metal center and the coordination environment.[72] According to chelation theory,

Table 4 Antibacterial activity of $(C_9H_8N)_2[ZnCl_4]\cdot 2H_2O$ compound (μg mL^{-1})

	QZnCl			CIP
Bacteria samples	MIC	MBC	$\frac{MBC}{MIC}$	MIC (μg mL^{-1})
Escherichia coli ATCC 25922	5	10	2	0.062
Pseudomonas aeruginosa ATCC 27583	5	10	2	0.125
Staphylococcus aureus ATCC 25923	5	10	2	0.031
Enterococcus faecalis ATCC 29212	10	20	2	0.125

complex formation reduces the polarity of the metal ion while increasing lipophilicity, thereby improving penetration through bacterial membranes and enabling effective disruption of essential cellular processes. Similar antibacterial effects (Table 4) have also been reported for quinoline-based zinc complexes, where activity was attributed to enhanced membrane interaction and intracellular targeting.[73]

Overall, these findings confirm the effectiveness of the $(C_9H_8N)_2[ZnCl_4]\cdot 2H_2O$ complex as a broad-spectrum bactericidal agent, in good agreement with previously reported zinc-based systems.

3.7 Biofilm inhibition effects

The antibiofilm activity of the $(C_9H_8N)_2[ZnCl_4]\cdot 2H_2O$ compound was also evaluated, revealing a strong inhibitory effect against all tested bacterial strains. At a concentration of 4× MIC, the inhibition percentage exceeded 70% in all cases, with the highest activity observed against *Pseudomonas aeruginosa* (85.69%, Fig. 19). The ability to inhibit biofilm formation is particularly significant, as biofilms are known to enhance bacterial resistance to conventional antibiotics.[74]

The observed antibiofilm performance can be attributed to the synergistic effect of Zn(II) coordination and the organic ligand, which enhances membrane interaction and disrupts bacterial adhesion processes. Similar behavior has been reported for zinc-based pyridine-derived complexes, where complexation improves penetration through the lipid bilayer and interferes with surface-associated biofilm formation. In addition, zinc chloride-based systems have demonstrated the ability to reduce biofilm formation by inhibiting bacterial adhesion and destabilizing the extracellular polymeric matrix, further supporting the role of zinc species in antibiofilm activity.[75]

Overall, these results indicate that the $(C_9H_8N)_2[ZnCl_4]\cdot 2H_2O$ complex exhibits significant antibacterial and antibiofilm properties, highlighting its potential as a multifunctional therapeutic agent.

3.8 Photoprotective study

The results demonstrate that the QZnCl complex absorbs between 250 and 320 nm, with SPF values of 4.2 ± 0.6 at 0.2 mg mL^{-1} and 6.5 ± 0.4 at 1 mg mL^{-1} (Table 5). The tested sample successfully blocks more than 80% of UV radiation at the high concentration (1 mg mL^{-1}), suggesting its overall sunscreen activity, when the extract's SPF value is compared to values in Table 5. It was previously claimed that strong electronic contacts between the ligand and Zn(II) center are confirmed by the distinctive $\pi-\pi^*$, $n-\pi^*$, and ligand-to-metal charge transfer transitions seen in the UV-vis spectra of Zn(II) complexes

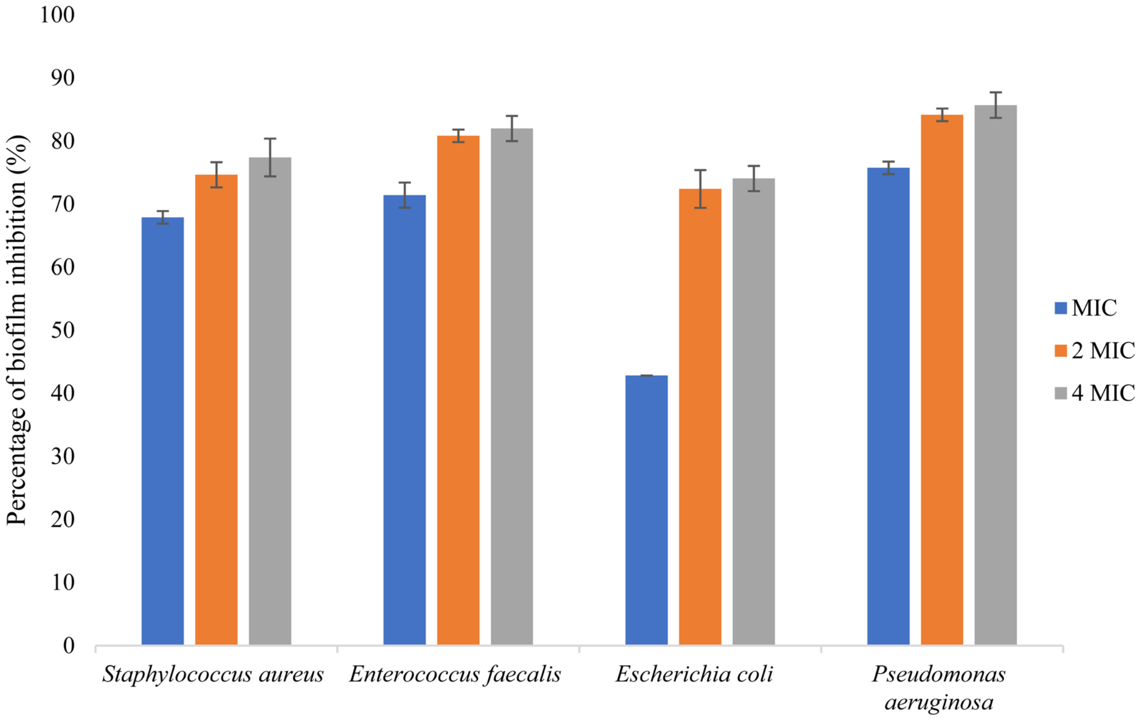

Fig. 19 Antibiofilm effect of $(C_9H_8N)_2[ZnCl_4]\cdot 2H_2O$.

Table 5 Results of photoprotective activity

Concentrations (mg mL^{-1})	SPF value
0.2	6.5 ± 0.4
1	4.2 ± 0.6

generated from quinoline. These changes increase the complexes' ability to absorb light, indicating that they may play a part in photoprotection through effective UV filtering.[76] Another paper confirmed that by increasing UV absorbance and stabilizing excited states, the photophysical characteristics of quinoline–Zn(II) complexes—specifically, their π–π*, n–π*, and LMCT transitions—support their prospective use as photoprotective agents.[77] It was previously reported that significant photophysical characteristics of quinoline-based Zn(II) complexes, such as high UV-vis absorption and fluorescence emission, are controlled by ligand–metal electronic interactions. These characteristics assist their prospective use in photoprotective systems by improving their capacity to absorb and disperse light energy.[78] Moreover, Zn(II) complex's UV-vis spectra show prominent absorption bands in the 229–258 nm region, which are ascribed to the quinoline moiety's π–π* transitions. A minor blue shift during complexation confirms the ligand–metal interaction.[79]

4 Conclusion

This study provides a comprehensive insight into the structure–property relationships of a quinolinium–zinc organic–inorganic hybrid system. Single-crystal X-ray diffraction analysis revealed a well-organized supramolecular architecture composed of isolated $[ZnCl_4]^{2-}$ tetrahedra interconnected with quinolinium cations and water molecules through an extended hydrogen-bonding network and π–π interactions, ensuring structural stability and compact packing. Vibrational and thermal analyses confirmed the integrity and robustness of the hybrid framework, while optical investigations demonstrated that the compound behaves as an indirect wide band gap semiconductor with an energy gap of approximately 3.02 eV. This behavior arises from the interplay between $\pi \rightarrow \pi^*$ transitions and ligand-to-metal charge transfer processes, highlighting the role of both organic and inorganic components in shaping the electronic structure. Theoretical calculations further supported the experimental findings, revealing a stable electronic configuration and moderate reactivity. In addition, *in silico* pharmacokinetic predictions indicated favorable absorption properties, while molecular docking studies showed moderate interactions with DNA gyrase and LasR proteins, providing a mechanistic interpretation of the observed biological activity. Importantly, the compound exhibited significant antibacterial and antibiofilm activities against both Gram-positive and Gram-negative strains, confirming its potential as a bioactive material. These findings demonstrate that the rational design of quinolinium–zinc hybrid systems offers a promising pathway toward multifunctional materials combining structural stability, semiconducting behavior, and biological performance.

Author contributions

Houyem Khlilfi: formal analysis, writing – original draft. Mashael A. Alghamdi: data curation, investigation. Intissar Tababi: data curation, validation. Hayet Edziri: conceptualization, data analysis. Marwa Melliti: formal analysis, investigation. Ahlem Guesmi: validation, software. Hossam H. Nasrallah: investigation, formal analysis. Noureddine Mhadhbi: methodology, investigation. Naoufel Ben Hamadi: formal analysis, writing – original draft. Houcine Naïli: project administration, review & editing.

Conflicts of interest

The authors declare that they have no known competing financial interests or personal relationships that could have appeared to influence the work reported in this paper.

Data availability

CCDC 2543095 contains the supplementary crystallographic data for this paper.[80]

The data that supported the findings of this study were available upon reasonable request.

Supplementary information (SI): structural, optical, and biological data of the zinc-based hybrid. See DOI: https://doi.org/10.1039/d6ra03131e.

Funding

This work was supported and funded by the Deanship of Scientific Research at Imam Mohammad Ibn Saud Islamic University (IMSIU) (grant number IMSIU-DDRSP2601).

References

1 F. Pantò, Z. Dahrouch, A. Saha, S. Patanè, S. Santangelo and C. Triolo, Photocatalytic degradation of methylene blue dye by porous zinc oxide nanofibers prepared via electrospinning: When defects become merits, *Appl. Surf. Sci.*, 2021, **557**, 149830, DOI: 10.1016/j.apsusc.2021.149830.

2 H. Chelghoum, N. Nasrallah, H. Tahraoui, M. F. Seleiman, M. M. Bouhenna, H. Belmeskine, M. Zamouche, S. Djema, J. Zhang, A. Mendil, F. Dergal, M. Kebir and A. Amrane, Eco-Friendly Synthesis of ZnO Nanoparticles for Quinoline Dye Photodegradation and Antibacterial Applications Using Advanced Machine Learning Models, *Catalysts*, 2024, **14**, 831, DOI: 10.3390/catal14110831.

3 J. Hemalatha, M. Senthil, A. M. Al-Mohaimeed and W. A. Al-onazi, Facile synthesis of activated carbon/ZnFe2O4 hybrid composite as an efficient photocatalyst for enhanced degradation of methylene blue (MB) and reactive red 120 dye under UV light, *J. Iran. Chem. Soc.*, 2024, **21**, 1317–1329, DOI: 10.1007/s13738-024-03000-2.

4 G. Velişa, Z. Fan, M. L. Crespillo, H. Bei, W. J. Weber and Y. Zhang, Temperature effects on damage evolution in ion-irradiated NiCoCr concentrated solid-solution alloy, *J.*

Alloys Compd., 2020, **832**, 154918, DOI: 10.1016/j.jallcom.2020.154918.

5 M. Doosti, R. Jahanshahi, S. Laleh, S. Sobhani and J. M. Sansano, Solar light induced photocatalytic degradation of tetracycline in the presence of ZnO/NiFe2O4/Co3O4 as a new and highly efficient magnetically separable photocatalyst, *Front. Chem.*, 2022, **10**, 1013349, DOI: 10.3389/fchem.2022.1013349.

6 S. Khan, A. Noor, I. Khan, M. Muhammad, M. Sadiq and N. Muhammad, Photocatalytic Degradation of Organic Dyes Contaminated Aqueous Solution Using Binary CdTiO2 and Ternary NiCdTiO2 Nanocomposites, *Catalysts*, 2022, **13**, 44, DOI: 10.3390/catal13010044.

7 H. Chelghoum, N. Nasrallah, H. Tahraoui, M. F. Seleiman, M. M. Bouhenna, H. Belmeskine, M. Zamouche, S. Djema, J. Zhang, A. Mendil, F. Dergal, M. Kebir and A. Amrane, Eco-Friendly Synthesis of ZnO Nanoparticles for Quinoline Dye Photodegradation and Antibacterial Applications Using Advanced Machine Learning Models, *Catalysts*, 2024, **14**, 831, DOI: 10.3390/catal14110831.

8 K. Ohkubo, T. Kobayashi and S. Fukuzumi, Direct Oxygenation of Benzene to Phenol Using Quinolinium Ions as Homogeneous Photocatalysts, *Angew. Chem., Int. Ed.*, 2011, **50**, 8652–8655, DOI: 10.1002/anie.201102931.

9 Y. Yamada, A. Nomura, T. Miyahigashi and S. Fukuzumi, Photocatalytic production of hydrogen peroxide by two-electron reduction of dioxygen with carbon-neutral oxalate using a 2-phenyl-4-(1-naphthyl)quinolinium ion as a robust photocatalyst, *Chem. Commun.*, 2012, **48**, 8329, DOI: 10.1039/c2cc34170k.

10 Y. Yamada, T. Miyahigashi, H. Kotani, K. Ohkubo and S. Fukuzumi, Photocatalytic Hydrogen Evolution under Highly Basic Conditions by Using Ru Nanoparticles and 2-Phenyl-4-(1-naphthyl)quinolinium Ion, *J. Am. Chem. Soc.*, 2011, **133**, 16136–16145, DOI: 10.1021/ja206079e.

11 Y. Yamada, T. Miyahigashi, H. Kotani, K. Ohkubo and S. Fukuzumi, Photocatalytic hydrogen evolution with Ni nanoparticles by using 2-phenyl-4-(1-naphthyl)quinolinium ion as a photocatalyst, *Energy Environ. Sci.*, 2012, **5**, 6111, DOI: 10.1039/c2ee03106j.

12 C.-Y. Yue, B. Hu, X.-W. Lei, R.-Q. Li, F.-Q. Mi, H. Gao, Y. Li, F. Wu, C.-L. Wang and N. Lin, Novel Three-Dimensional Semiconducting Materials Based on Hybrid d 10 Transition Metal Halogenides as Visible Light-Driven Photocatalysts, *Inorg. Chem.*, 2017, **56**, 10962–10970, DOI: 10.1021/acs.inorgchem.7b01171.

13 F. Temerov, Y. Baghdadi, E. Rattner and S. Eslava, A Review on Halide Perovskite-Based Photocatalysts: Key Factors and Challenges, *ACS Appl. Energy Mater.*, 2022, **5**, 14605–14637, DOI: 10.1021/acsaem.2c02680.

14 J. Luo, W. Zhang, H. Yang, Q. Fan, F. Xiong, S. Liu, D. Li, B. Liu, *Halide Perovskite Composites for Photocatalysis: A Mini Review*, EcoMat, 2021, Vol. 3, DOI: 10.1002/eom2.12079.

15 K. A. Huynh, D. L. T. Nguyen, V. Nguyen, D. N. Vo, Q. T. Trinh, T. P. Nguyen, S. Y. Kim and Q. Van Le, Halide perovskite photocatalysis: progress and perspectives, *J. Chem. Technol. Biotechnol.*, 2020, **95**, 2579–2596, DOI: 10.1002/jctb.6342.

16 C. Ayari, A. A. Alotaibi, M. A. Baashen, F. Perveen, A. H. Almarri, K. M. Alotaibi, M. S. M. Abdelbaky, S. Garcia-Granda, A. Othmani, C. Ben Nasr and M. H. Mrad, A New Zn(II) Metal Hybrid Material of 5-Nitrobenzimidazolium Organic Cation (C7H6N3O2)2[ZnCl4]: Elaboration, Structure, Hirshfeld Surface, Spectroscopic, Molecular Docking Analysis, Electric and Dielectric Properties, *Materials*, 2022, **15**, 7973, DOI: 10.3390/ma15227973.

17 J.-W. Li, W. Dong, Y. Liu, Y. Li, L.-Y. Qiao, G.-L. Liu, H. Zhang, C. Wang, H.-L. Zheng and J.-Q. Zhao, Water-stable zero-dimensional hybrid zinc halide modulated by π–π interactions: efficient blue light emission and third-order nonlinear optical response, *Inorg. Chem. Front.*, 2024, **11**, 8431–8438, DOI: 10.1039/D4QI02194K.

18 V. A. Online, *RSC Adv.*, 2016, 59055–59065, DOI: 10.1039/c6ra09630a.

19 N. Loulou, W. Rekik, T. Mhiri, K. T. Mahmudov, M. N. Kopylovich and H. Naïli, Inorganica Chimica Acta selenates (M II = Co II, Ni II, Cu II, Zn II) as effective catalysts for Henry reaction, *Inorg. Chim. Acta*, 2024, **412**, 27–31, DOI: 10.1016/j.ica.2013.12.007.

20 W. Rekik, H. Na, T. Mhiri and T. Bataille, A new dabco templated metal sulfate, $(C_6H_{14}N_2)[Mn(H_2O)_6](SO_4)_2$. Chemical preparation, hydrogen-bonded structure and thermal decomposition, *J. Chem. Crystallogr.*, 2007, **37**, 147–155.

21 H. Tllili, S. Walha, S. Elleuch, B. Fares and H. Naïli, Structural, vibrational, DFT and optical studies of a new non- centrosymmetric hybrid material (C 4 H 12 N 2)[CoBr 4], *J. Mol. Struct.*, 2018, **1152**, 303–310, DOI: 10.1016/j.molstruc.2017.09.096.

22 I. Ben Mahmoud, N. Ben Hamadi, S. Walha, N. Zammel, A. Ben Ahmed, A. Guesmi, W. Abd El-Fattah, F. Costantino and H. Naïli, Structural, Optical and Biological Characterization of a New Cobalt-Based Mixed Halide Hybrid Compound: Insights from DFT and Vibrational Analysis, *R. Soc. Open Sci.*, 2025, **12**, 250485, DOI: 10.1098/rsos.250485.

23 I. Hamdi, Y. Khan, F. Aouaini, J. H. Seo, H.-J. Koo, M. M. Turnbull, B. Walker and H. Naïli, A copper-based 2D hybrid perovskite solar absorber as a potential eco-friendly alternative to lead halide perovskites, *J. Mater. Chem. C*, 2022, **10**, 3738–3745, DOI: 10.1039/d1tc05047h.

24 M. Abid, M. M. Turnbull, H. Naïli and W. Rekik, A new mixed halide 2D hybrid perovskite : Structural , thermal , optic and magnetic properties, *Polyhedron*, 2020, **175**, 114220, DOI: 10.1016/j.poly.2019.114220.

25 R. Martinez-Haya, C. Sabater, M.-Á. Castillo, M. A. Miranda and M. L. Marin, A mechanistic study on the potential of quinolinium salts as photocatalysts for the abatement of chlorinated pollutants, *J. Hazard. Mater.*, 2018, **351**, 277–284, DOI: 10.1016/j.jhazmat.2018.03.010.

26 K. Ohkubo, T. Kobayashi and S. Fukuzumi, Direct Oxygenation of Benzene to Phenol Using Quinolinium Ions

as Homogeneous Photocatalysts, *Angew. Chem., Int. Ed.*, 2011, **50**, 8652–8655, DOI: 10.1002/anie.201102931.

27 Y. Yamada, A. Nomura, T. Miyahigashi and S. Fukuzumi, Photocatalytic production of hydrogen peroxide by two-electron reduction of dioxygen with carbon-neutral oxalate using a 2-phenyl-4-(1-naphthyl)quinolinium ion as a robust photocatalyst, *Chem. Commun.*, 2012, **48**, 8329, DOI: 10.1039/c2cc34170k.

28 S. Ru, C.-C. Zhao, Z. Wu, L.-K. Yan, D. Zang and Y. Wei, Molecular Photocatalysts Based on Quinolinium-Grafted Polyoxometalates for Efficient One-Step Aerobic Oxidation of Benzyl Alcohols to Benzoic Acids, *ACS Sustain. Chem. Eng.*, 2024, **12**, 6827–6839, DOI: 10.1021/acssuschemeng.3c05573.

29 R. C. Clark and J. S. Reid, The analytical calculation of anisotropic displacement parameters for molecular crystals, *Acta Crystallogr., Sect. A*, 1995, **51**, 887–897, DOI: 10.1107/S0108767395007367.

30 M. Kashkouli and J. Khajehali, Obligate and facultative symbionts in different populations of the greenhouse whitefly, Trialeurodes vaporariorum (Hem.: Aleyrodidae), *J. Entomol. Soc. Iran*, 2024, **44**, 1–10, DOI: 10.61186/jesi.44.1.1.

31 L. Hu, P. Yin, G. H. Imler, D. A. Parrish, H. Gao and J. M. Shreeve, Fused rings with N-oxide and -NH2: Good combination for high density and low sensitivity energetic materials, *Chem. Commun.*, 2019, **55**, 8979–8982, DOI: 10.1039/c9cc04496e.

32 L. J. Farrugia, WinGX and ORTEP for Windows: An update, *J. Appl. Crystallogr.*, 2012, **45**, 849–854, DOI: 10.1107/S0021889812029111.

33 G. M. Sheldrick, *Crystal Structure Refinement with SHELXL*, 2014, pp. 3–8, DOI: 10.1107/S2053229614024218.

34 F. Paquin, J. Rivnay, A. Salleo, N. Stingelin and C. Silva, Multi-phase semicrystalline microstructures drive exciton dissociation in neat plastic semiconductors, *J. Mater. Chem. C*, 2015, **3**, 10715–10722, DOI: 10.1039/b000000x.

35 B. G. Janesko, Replacing hybrid density functional theory: motivation and recent advances, *Chem. Soc. Rev.*, 2021, **50**, 8470–8495, DOI: 10.1039/D0CS01074J.

36 A. M. Abbas, A. Aboelmagd, S. M. Kishk, H. H. Nasrallah, W. C. Boyd, H. Kalil and A. S. Orabi, A Novel Ibuprofen Derivative and Its Complexes: Physicochemical Characterization, DFT Modeling, Docking,In Vitro Anti-Inflammatory Studies, and DNA Interaction, *Molecules*, 2022, **27**(21), 29, DOI: 10.3390/molecules27217540.

37 A. M. Abbas, H. H. Nasrallah, A. Aboelmagd, S. M. Kishk, W. C. Boyd, H. Kalil and A. S. Orabi, Design, Synthesis, Anti-Inflammatory Activity, DFT Modeling and Docking Study of New Ibuprofen Derivatives, *Int. J. Mol. Sci.*, 2024, **25**, 3558.

38 A. Daina, O. Michielin and V. Zoete, SwissADME: a free web tool to evaluate pharmacokinetics, drug-likeness and medicinal chemistry friendliness of small molecules, *Sci. Rep.*, 2017, **7**, 42717, DOI: 10.1038/srep42717.

39 H. M. Berman, The Protein Data Bank, *Nucleic Acids Res.*, 2000, **28**, 235–242, DOI: 10.1093/nar/28.1.235.

40 F. Agili, Novel Thiazole Derivatives Containing Imidazole and Furan Scaffold: Design, Synthesis, Molecular Docking, Antibacterial, and Antioxidant Evaluation, *Molecules*, 2024, **29**, 1491, DOI: 10.3390/molecules29071491.

41 G. M. Morris, R. Huey, W. Lindstrom, M. F. Sanner, R. K. Belew, D. S. Goodsell and A. J. Olson, AutoDock4 and AutoDockTools4: Automated docking with selective receptor flexibility, *J. Comput. Chem.*, 2009, **30**, 2785–2791, DOI: 10.1002/jcc.21256.

42 O. Trott and A. J. Olson, AutoDock Vina: Improving the speed and accuracy of docking with a new scoring function, efficient optimization, and multithreading, *J. Comput. Chem.*, 2010, **31**, 455–461, DOI: 10.1002/jcc.21334.

43 A. M. Abbas, A. Aboelmagd, S. M. Kishk, H. H. Nasrallah, W. C. Boyd, H. Kalil and A. S. Orabi, A Novel Ibuprofen Derivative and Its Complexes: Physicochemical Characterization, DFT Modeling, Docking, In Vitro Anti-Inflammatory Studies, and DNA Interaction, *Molecules*, 2022, **27**, 7540.

44 A. M. Abbas, H. H. Nasrallah, A. Aboelmagd, S. M. Kishk, W. C. Boyd, H. Kalil and A. S. Orabi, Design, Synthesis, Anti-Inflammatory Activity, DFT Modeling and Docking Study of New Ibuprofen Derivatives, *IJMS*, 2024, **25**, 3558, DOI: 10.3390/ijms25063558.

45 PyMOL | pymol.org, (n.d.). https://pymol.org/(accessed April 8, 2026).

46 M. Melliti, E. M. Musa, M. Horchani and M. Santana, all Aspects of Plant Biology Chemical composition , antimicrobial and anticoagulant potentials of microencapsulated essential oil from Centaurea bimorpha (Asteraceae), and in silico study, *Plant Biosyst.*, 2025, **0**, 1–16, DOI: 10.1080/11263504.2025.2466574.

47 H. Edziri, R. Jaziri, H. Chehab, L. Verschaeve and G. Flamini, Heliyon A comparative study on chemical composition , antibio fi lm and biological activities of leaves extracts of four Tunisian olive cultivars, *Heliyon*, 2019, **5**, e01604, DOI: 10.1016/j.heliyon.2019.e01604.

48 M. Ali, N. El, H. Ben, M. Haj, A. Faidi, H. Majdoub and S. Sfar, European Journal of Integrative Medicine Photoprotective potential of a Tunisian halophyte plant Carpobrotus edulis L, *Eur. J. Integr. Med.*, 2021, **42**, 101286, DOI: 10.1016/j.eujim.2021.101286.

49 J. S. Mansur, M. N. R. Breder, M. C. A. Mansur and R. D. Azulay, Determination of Sun Protection Factor by Spectrophotometry, *An. Bras. Dermatol.*, 1986, **61**, 121–124.

50 S. Ram, The influence of hydrogen bonding on the character of N—H and C═O stretching modes in 2-thiopyrrole-1,2-dicarboximide, *Can. J. Chem.*, 1984, **62**, 1845–1849, DOI: 10.1139/v84-316.

51 A. Thander, D. Basak and B. Mallik, Spectroscopic studies on the photoeffects on some metallocenes in the presence of chloroform molecules confined in poly(methyl methacrylate) thin films, *Spectrochim. Acta, Part A*, 2004, **60**, 2393–2398, DOI: 10.1016/j.saa.2003.12.014.

52 J. Danon and L. Iannarella, Mössbauer Hyperfine Interactions in Sodium Nitroprusside Single Crystals, *J. Chem. Phys.*, 1967, **47**, 382–387, DOI: 10.1063/1.1711904.

53 M. Debeau and R. M. Pick, Spectres de Diffusion Raman d'un Monocristal de CBr 4 Monoclinique, *J. Raman Spectrosc.*, 1980, **9**, 157–161, DOI: 10.1002/jrs.1250090306.

54 F. Pickhard and H. Hartl, Die Kristallstrukturen von K 8 Ta 6 O 19 · 16H 2 O und K 7 NaTa 6 O 19 · 14H 2 O, *Z. Anorg. Allg. Chem.*, 1997, **623**, 1311–1316, DOI: 10.1002/zaac.19976230823.

55 M. Arita and H.-U. Nissen, Electron Microscopy of the "Disordered Phase" in Nb-Ge Thin Films, *J. Solid State Chem.*, 1993, **106**, 427–442, DOI: 10.1006/jssc.1993.1303.

56 J. Xue, Z. Wang, A. Comstock, Z. Wang, H. H. Y. Sung, I. D. Williams, D. Sun, J. Liu and H. Lu, Chemical Control of Magnetic Ordering in Hybrid Fe – Cl Layered Double Perovskites, *Chem. Mater.*, 2022, **34**(6), 2813–2823, DOI: 10.1021/acs.chemmater.2c00163.

57 H. Tllili, S. Walha, S. Elleuch, B. Fares and H. Naili, Structural, vibrational, DFT and optical studies of a new non-centrosymmetric hybrid material $(C_4H_{12}N_2)$[CoBr4], *J. Mol. Struct.*, 2018, **1152**, 303–310, DOI: 10.1016/j.molstruc.2017.09.096.

58 G. Ferraro, N. Demitri, L. Vitale, G. Sciortino, D. Sanna, V. Ugone, E. Garribba and A. Merlino, Spectroscopic/Computational Characterization and the X - Ray Structure of the Adduct of the VIVO–picolinato complex with RNase A, *Inorg. Chem.*, 2021, **60**, 19098–19109, DOI: 10.1021/acs.inorgchem.1c02912.

59 F. Hcini, J. Khelifi and K. Khirouni, Enhanced Electrical , Optical and Thermodynamics Proprieties of - Pr 0.5 Ce 0.5 CoO 3 Cobaltite Prepared Using Sol – Gel Route for Electrical and Optical Applications, *J. Inorg. Organomet. Polym. Mater.*, 2023, **33**, 3178–3194, DOI: 10.1007/s10904-023-02739-0.

60 N. A. Ahmed, H. Hammache, L. Makhloufi, M. Eyraud, S. Sam and N. Gabouze, *Effect of Electrodeposition Duration on the Morphological and Structural Modification of the Flower-like Nanostructured ZnO*, 2020.

61 P. Properties, O. Z. Nanostructures, A. Bouzidi, H. Algarni, H. Y. Zahran and M. S. Abdel-wahab, *Enhancement in the Structural, Electrical, Optical, and Photocatalytic Properties of La 2 O 3 -Doped ZnO Nanostructures*, 2022.

62 V. N. Bakunin, G. N. Kuzmina and O. P. Parenago, *Recent Achievements in Synthesis and Application of Inorganic Nanoparticles as Lubricant*, 2004.

63 N. Tounsi, A. Barhoumi, F. C. Akkari, M. Kanzari, H. Guermazi and S. Guermazi, Structural and optical characterization of copper oxide composite thin fi lms elaborated by GLAD technique, *Vacuum*, 2015, **121**, 9–17, DOI: 10.1016/j.vacuum.2015.07.011.

64 S. R. Chalana, V. Ganesan and V. P. M. Pillai, Surface Plasmon Resonance in Nanostructured Ag Incorporated ZnS Films, *AIP Adv.*, 2015, **5**, 107207, DOI: 10.1063/1.4933075.

65 D. F. Veber, S. R. Johnson, H.-Y. Cheng, B. R. Smith, K. W. Ward and K. D. Kopple, Molecular Properties That Influence the Oral Bioavailability of Drug Candidates, *J. Med. Chem.*, 2002, **45**, 2615–2623, DOI: 10.1021/jm020017n.

66 E. F. Plinski and S. Plinska, Veber's Rules in Terahertz Light, *Research Square*, 2020, DOI: 10.21203/rs.2.22281/v1.

67 D. E. V. Pires, T. L. Blundell and D. B. Ascher, pkCSM: Predicting Small-Molecule Pharmacokinetic and Toxicity Properties Using Graph-Based Signatures, *J. Med. Chem.*, 2015, **58**, 4066–4072, DOI: 10.1021/acs.jmedchem.5b00104.

68 T. Damena, T. Desalegn, S. Mathura, A. Getahun, D. Bizuayehu, M. B. Alem, S. Gadisa, D. Zeleke and T. B. Demissie, Synthesis, Structural Characterization, and Computational Studies of Novel Co(II) and Zn(II) Fluoroquinoline Complexes for Antibacterial and Antioxidant Activities, *ACS Omega*, 2024, **9**, 36761–36777, DOI: 10.1021/acsomega.4c05560.

69 D. Dinku, T. B. Demissie, I. N. Beas and T. Desalegn, Synthesis, Molecular Docking, and antibacterial evaluation of Quinoline-Derived Ni(II), Cu(II) and Zn(II) complexes, *Results Chem.*, 2024, **8**, 101562, DOI: 10.1016/j.rechem.2024.101562.

70 G. Shumi, T. B. Demissie, G. Kenasa, A. Lealem Birhanu, I. N. Beas and T. Desalegn, Synthesis, characterization, antibacterial, antioxidant and molecular docking studies of Zn(II) complexes with imine quinoline derivative ligand, *Inorg. Chem. Commun.*, 2024, **170**, 113304, DOI: 10.1016/j.inoche.2024.113304.

71 T. H. Al-noor, M. R. Aziz and A. T. A. Jeboori, Research Article Synthesis, characterization and antimicrobial activities of [Fe (II), Co (II), Ni (II), Cu (II) and Zn (II)] mixed ligand complexes schiff base derived from amoxicillin drug and 4-(dimethylamino) benzaldehyde with nicotinamide, *J. Chem. Pharm. Res.*, 2014, **6**(4), 1225–1231.

72 K. Azeem, S. Fatima, A. Ali, A. Ubaid, F. M. Husain and M. Abid, Biochemistry of Bacterial Biofilm : Insights into Antibiotic Resistance Mechanisms and Therapeutic Intervention, *Life*, 2025, **15**(1), 49, DOI: 10.3390/life15010049.

73 D. Dinku, T. B. Demissie, I. N. Beas and T. Desalegn, Results in Chemistry Synthesis , Molecular Docking , and antibacterial evaluation of Quinoline-Derived Ni (II), Cu (II) and Zn (II) complexes, *Results Chem.*, 2024, **8**, 101562, DOI: 10.1016/j.rechem.2024.101562.

74 L. Xue, X. Fu, G. Zhao and Q. Li, Zinc (II) Complexes Derived from Schiff Bases: Syntheses, Structures, and Biological Activity, *Acta Chim. Slov.*, 2021, **68**(1), 17–24, DOI: 10.17344/acsi.2020.5817.

75 N. Noach, E. Lavy, R. Reifen, M. Friedman, D. Kirmayer, E. Zelinger, A. Ritter, D. Yaniv and E. Reifen, Zinc chloride is effective as an antibiotic in biofilm prevention following septoplasty, *Sci. Rep.*, 2023, 1–12, DOI: 10.1038/s41598-023-35069-9.

76 D. Dinku, T. B. Demissie, I. N. Beas and T. Desalegn, Results in Chemistry Synthesis , Molecular Docking , and antibacterial evaluation of Quinoline-Derived Ni (II), Cu (II) and Zn (II) complexes, *Results Chem.*, 2024, **8**, 101562, DOI: 10.1016/j.rechem.2024.101562.

77 S. K. Alharbi, S. M. Alahmadi, I. Omar, M. M. Khashoqji, F. S. Aljohani, I. O. Barnawi, M. Fathalla, S. A. Abdel-latif, M. Salaheldeen and A. M. Abu-dief, Design of Quinoline-

Derived Schiff Base Metal Complexes as Bioactive Drug Candidates: Structural Elucidation, Stability Determination, DFT, and Docking Studies with DNA-Targeting Potential Profiles, *Int. J. Mol. Sci.*, 2026, **27**(4), 1828, DOI: 10.3390/ijms27041828.

78 A. A. Andelescu, A. Candreva, E. Popa, A. Visan and C. Cretu, Role of the Environment Polarity on the Photophysical Properties of Mesogenic Hetero-Polymetallic Complex, *Molecules*, 2024, **29**(4), 750, DOI: 10.3390/molecules29040750.

79 T. Damena, M. B. Alem, D. Zeleke, T. Desalegn, R. Eswaramoorthy and T. B. Demissie, Biological Activities of Zinc (II), Copper (II) and Nickel (II) Complexes of an Aminoquinoline Derivative, *Front. Chem.*, 2022, **10**, 1053532, DOI: 10.3389/fchem.2022.1053532.

80 CCDC 2543095: Experimental Crystal Structure Determination, 2026, DOI: 10.5517/ccdc.csd.cc2rc9bs.